

1 **Statistics and Forecasting of Aftershocks during the**
2 **2019 Ridgecrest, California, Earthquake Sequence**

3 **Robert Shcherbakov^{1,2}**

4 ¹Department of Earth Sciences, University of Western Ontario, London, Ontario, *N6A 5B7*, Canada.

5 ²Department of Physics and Astronomy, University of Western Ontario, London, Ontario, *N6A 3K7*,
6 Canada.

7 **Key Points:**

- 8 • Statistical analysis of the 2019 Ridgecrest, California, earthquake sequence is per-
9 formed.
- 10 • The probabilities for the occurrence of the largest expected aftershocks are com-
11 puted using the Bayesian predictive framework.
- 12 • The aftershock forecast is verified retrospectively using several statistical tests.

Abstract

The 2019 Ridgecrest, California, earthquake sequence represents a complex pattern of seismicity that is characterized by the occurrence of a well defined foreshock sequence followed by a mainshock and subsequent aftershocks. In this work, a detailed statistical analysis of the sequence is performed. Particularly, the parametric modelling of the frequency-magnitude statistics and the earthquake occurrence rate is carried out. It is shown that the clustering of earthquakes plays an important role during the evolution of this sequence. In addition, the problem of constraining the magnitude of the largest expected aftershocks to occur during the evolution of the sequence is addressed. In order to do this, two approaches are considered. The first one is based on the extreme value theory, whereas the second one uses the Bayesian predictive framework. The latter approach has allowed to incorporate the complex earthquake clustering through the Epidemic Type Aftershock Sequence (ETAS) process and the uncertainties associated with the model parameters into the computation of the corresponding probabilities. The results indicate that the inclusion of the foreshock sequence into the analysis produces higher probabilities for the occurrence of the largest expected aftershocks after the M7.1 mainshock compared to the approach based on the extreme value distribution combined with the Omori-Utsu formula for the earthquake rate. Several statistical tests are applied to verify the forecast.

Plain Language Summary

Strong earthquakes typically trigger the subsequent sequence of events known as aftershocks. Among those, the largest aftershocks can pose significant hazard and result in additional damage to already weakened by the mainshock infrastructure. Therefore, the estimation of the magnitude of the largest expected aftershock is of critical importance. This problem can be addressed within the statistical modelling of the occurrence of earthquakes. In this work, the 2019 Ridgecrest, California, earthquake sequence is chosen to illustrate and compare several approaches as to how these probabilities can be computed during the evolution of the sequence. The first approach uses the extreme value theory and the modelling of the earthquake rate based on the Omori-Utsu formula. Whereas, the second approach uses a recently formulated method based on the Bayesian predictive analysis and the Epidemic Type Aftershock Sequence (ETAS) model to approximate the earthquake rate. The obtained results indicate that the latter approach produces sta-

45 tistically accurate forecast for the magnitudes of the largest expected earthquakes. This
46 is verified by applying several statistical tests.

47 **1 Introduction**

48 The occurrence of a significant mainshock presents an opportunity to test differ-
49 ent existing or novel statistical approaches to model the evolution of the corresponding
50 sequences of earthquakes that precede and follow the mainshock. Among several statis-
51 tical measures, the computation of the probability to have the magnitude of the largest
52 expected earthquake to be above a certain value during a predefined future time inter-
53 val is of critical importance. In this respect, the 2019 Ridgecrest, California, earthquake
54 sequence represents the latest highly productive and non-standard sequence to be an-
55 alyzed in detail.

56 The 2019 Ridgecrest sequence started on July 4th when several small events of low
57 magnitude occurred not far away from the town of Ridgecrest in southern California. Then,
58 two strong foreshocks of magnitudes M3.98 and M6.4 struck on 2019/07/04 at 17:02:55
59 UTC and 17:33:49 UTC, respectively (Figure 1). These events were followed by a well-
60 developed aftershock sequence that culminated in the occurrence of M7.1 mainshock on
61 2019/07/06 (03:19:53 UTC), which in turn generated a more prolific aftershock sequence.
62 The M6.4 foreshock ruptured several predominantly strike-slip, left-lateral fault segments,
63 whereas the M7.1 mainshock occurred on a system of several right-lateral fault segments
64 conjugate to the rupture of the M6.4 foreshock (Ross et al., 2019; Barnhart et al., 2019).
65 Many of the foreshocks and subsequent aftershocks of the M7.1 mainshock occurred on
66 numerous secondary faults adjacent to the main rupture faults. It was suggested that
67 this earthquake sequence occurred in an immature fault zone with a complex fault struc-
68 ture (Ross et al., 2019; Liu et al., 2019).

69 In this paper, a detailed statistical analysis of the 2019 Ridgecrest earthquake se-
70 quence was performed to study its temporal evolution and frequency-magnitude statis-
71 tics. In addition, several methods were considered to estimate the probabilities to have
72 the largest expected aftershock to be above a certain magnitude during several stages
73 of the evolution of the sequence. The computation of probabilities was performed using
74 two approaches, i.e., the one based on the extreme value theory and the second one us-
75 ing the Bayesian predictive distribution. These approaches assume parametric models

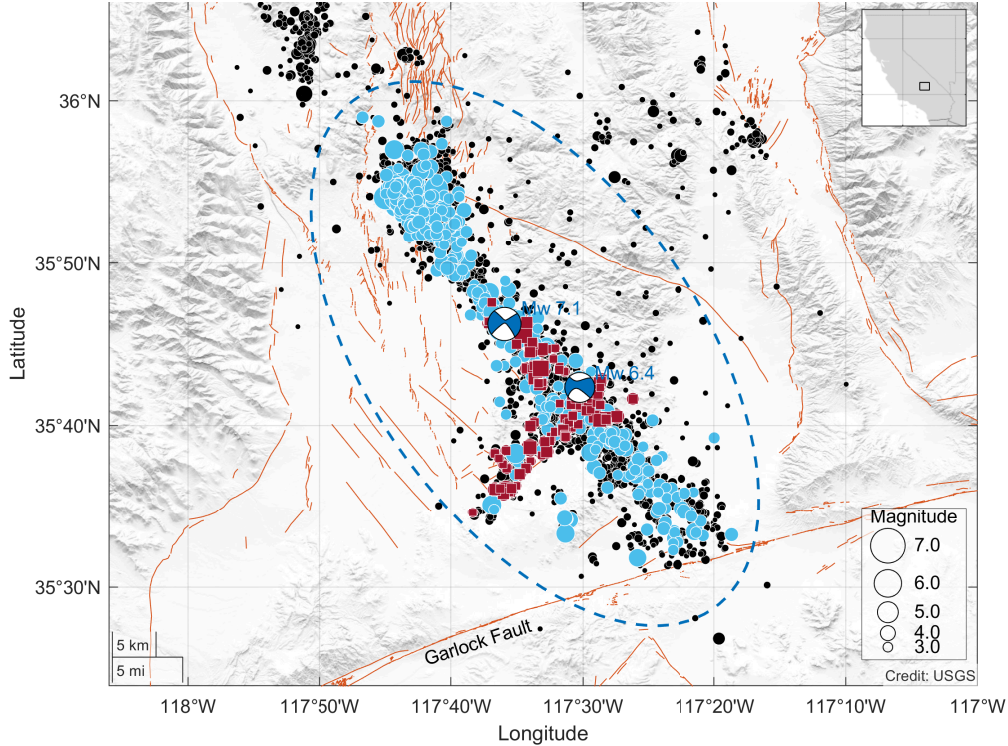


Figure 1. The distribution of earthquake epicenters of the 2019 Ridgecrest, California, sequence during 14 days starting from 2019/07/04 (17:02:55 UTC). Solid squares within an elliptical zone indicate foreshocks above magnitude $m \geq 3.2$ during 1.428 days before the occurrence of the M7.1 mainshock on 2019/07/06 (03:19:53 UTC). Similarly, solid circles indicate aftershocks of the M7.1 mainshock. The focal mechanisms of the M7.1 mainshock and M6.4 foreshock are plotted as beach balls. All other earthquakes above magnitude $m \geq 2.0$ are shown as black solid circles. The quaternary faults are plotted as light brown line segments.

76 for the earthquake occurrence rate and the frequency-magnitude statistics. Specifically,
 77 the Omori-Utsu (OU) law (Omori, 1894; Utsu, 1961; Utsu et al., 1995), the compound
 78 Omori-Utsu law (Ogata, 1983), and the Epidemic Type Aftershock Sequence (ETAS)
 79 process (Ogata, 1988, 1999, 2017) were used to approximate the earthquake rate. The
 80 frequency-magnitude statistics of earthquakes was modelled by the left-truncated expo-
 81 nential distribution (Vere-Jones, 2010). The obtained results, which are reported below,
 82 suggest that the clustering of earthquakes plays an important role in approximating the
 83 earthquake rate and as a consequence can significantly affect the computation of the prob-
 84 abilities for the occurrence of the largest expected aftershocks.

85 The problem of constraining the magnitudes of the largest expected aftershocks is
86 important as these aftershocks can inflict further damage to already weakened by a main-
87 shock structures or the evolution of the sequence can trigger even larger subsequent events
88 (Gerstenberger et al., 2005; Shebalin et al., 2011; Omi et al., 2013; Page et al., 2016).
89 The standard approach is to use the past seismicity to compute the probabilities of hav-
90 ing subsequent strong earthquakes during a finite future time interval. The most recog-
91 nized model was formulated by Reasenber and Jones (1989) for California based on the
92 analysis of the past aftershock sequences. In that model, the probabilities are computed
93 from the extreme value distribution by assuming that the occurrence of earthquakes fol-
94 lows a non-homogeneous Poisson process, the earthquake rate is approximated by the
95 Omori-Utsu formula and the frequency-magnitude statistics is described by the left-truncated
96 exponential distribution. Reasenber and Jones (1989) estimated the average values of
97 the model parameters to be used in California. However, a recent work by Hardebeck
98 et al. (2019) introduced improvements to the original Reasenber and Jones (1989) model
99 by analysing more recent sequences, introducing the ability to control the early incom-
100 pleteness of aftershock sequences, and using the Bayesian updating of the model param-
101 eters. These developments contributed to the introduction of the operational aftershock
102 forecasting in the U.S. by the U.S. Geological Survey (Michael et al., 2019). A similar
103 approach has been undertaken in Japan to create a real-time system for automatic af-
104 tershock forecasting (Omi et al., 2016, 2019). Earthquake forecasting centers also op-
105 erate in New Zealand (Rhoades et al., 2018) and Italy (Taroni et al., 2018), where the
106 evaluation of earthquake probabilities and assessment of earthquake hazard are routinely
107 performed.

108 A critical aspect of any earthquake forecasting methods is their prospective/retrospective
109 testing and validation (Kagan & Jackson, 1995). This is consistently implemented by
110 the Collaboratory for the Study of Earthquake Predictability (CSEP) (Schorlemmer et
111 al., 2007; Zechar et al., 2010; Schorlemmer et al., 2018; Gerstenberger et al., 2020). Within
112 the CSEP framework several statistical methods were developed to test the short/long
113 term earthquake forecasts. Those methods test the consistency of a given forecasting scheme
114 to reproduce the observed number of earthquakes, their spatial and magnitude distri-
115 butions during the forecasting time interval (Zechar et al., 2010). They also incorporate
116 likelihood based approaches to compare various forecasting schemes. For example, this
117 framework was used to test the performance of aftershock forecasts during the 2011 To-

118 hoku, Japan, earthquake (Nanjo et al., 2012), the 2010 Canterbury, New Zealand, earth-
119 quake sequence (Rhoades et al., 2016; Cattania et al., 2018), and the 2016 Kaikoura, New
120 Zealand, earthquake sequence (Rhoades et al., 2018).

121 An early systematic empirical study of aftershocks concluded that the largest oc-
122 curred aftershock on average was approximately 1.2 magnitude less than the magnitude
123 of a mainshock (Båth, 1965). This is referred to as Båth’s law. Subsequently, it was pro-
124 posed that the difference was independent of the number of events and its mean value
125 was proportional to the inverse of the b -value (Vere-Jones, 1969, 1975). More recent stud-
126 ies have provided further details on this difference (Console et al., 2003; Shcherbakov &
127 Turcotte, 2004; Tahir et al., 2012; Shearer, 2012; Shcherbakov et al., 2013). The after-
128 shock sequences also exhibit scaling with respect to the lower magnitude cutoff (Shcherbakov
129 et al., 2004; Shcherbakov, Turcotte, & Rundle, 2005; Shcherbakov et al., 2006, 2015).

130 An important limitation of all earthquake catalogs is the early aftershock incom-
131 pleteness (Kagan, 2004; Peng et al., 2006; Hainzl, 2016b, 2016a). This incompleteness
132 can affect the estimation of the model parameters if the magnitude of completeness is
133 underestimated. As a result, this can significantly influence the calculation of the prob-
134 abilities for the occurrence of extreme earthquakes. To recover partially the true rate a
135 variable magnitude of completeness can be considered (Helmstetter et al., 2006; Omi et
136 al., 2014; Page et al., 2016). Several approaches were suggested to recover the aftershock
137 rate by using the information of early aftershocks in order to estimate the probability
138 of larger subsequent events during future evolution of the sequences (Omi et al., 2013;
139 Ebrahimian et al., 2014; Omi et al., 2016).

140 The occurrence of strong earthquakes typically produces spatial and temporal clus-
141 ters. This clustering is a result of triggering by preceding earthquakes that can lead to
142 a cascade of events with a complicated branching structure (Felzer et al., 2004). To de-
143 scribe such a clustering, the ETAS model was introduced that offers a realistic and quan-
144 tifiable approximation to the earthquake occurrence rate (Ogata, 1988, 1999, 2017). Par-
145 ticularly, it can model the rate of earthquakes punctuated by the occurrence of strong
146 earthquakes. This also allows to quantify the increased earthquake hazard after a main-
147 shock by incorporating the triggering ability of foreshocks, a mainshock, and subsequent
148 aftershocks. It also can be used for short-term forecasting of large earthquakes by study-

149 ing past seismicity (Helmstetter et al., 2006; Ogata, 2017; Ebrahimian & Jalayer, 2017;
 150 D. S. Harte, 2017; Omi et al., 2019).

151 The paper is organized as follows. In Section Methods, the statistical methods used
 152 in the study are summarized and explained. In Section Results, a detailed analysis of
 153 the sequence is presented. In Section Discussion, the obtained results are summarized
 154 and evaluated. The last section presents concluding remarks.

155 2 Methods

156 2.1 Earthquake Catalog and the Spatial Distribution of Seismicity

157 To analyze the 2019 Ridgecrest earthquake sequence, the earthquake catalog pro-
 158 vided by the Southern California Seismic Network (SCSN) was used. The spatial dis-
 159 tribution of seismicity during 14 days starting from 2019/07/04 (17:02:55 UTC) is shown
 160 in Figure 1. This includes the occurrence of the M6.4 foreshock on 2019/07/04 (17:33:49
 161 UTC) and the occurrence of the M7.1 mainshock on 2019/07/06 (03:19:53 UTC). Their
 162 focal mechanisms are also shown and were obtained from the SCSN Moment Tensor cat-
 163 alog. The foreshock-aftershock zone for the sequence is defined as an elliptical region out-
 164 lining the majority of earthquakes that occurred near the ruptures of both the M6.4 fore-
 165 shock and M7.1 mainshock. Figure 1 also shows the quaternary faults for this region ex-
 166 tracted from the U.S.G.S. Quaternary fault and fold database.

167 When analyzing seismicity, several time intervals, during which the parameters of
 168 statistical models can be estimated or future evolution of the seismicity can be quanti-
 169 fied, are defined. Specifically, the past seismicity is extracted during the *training time*
 170 *interval* $[T_0, T_e]$. To minimize the effect of earlier earthquakes in the sequence, the train-
 171 ing time interval is typically subdivided into a preparatory time interval $[T_0, T_s]$ and a
 172 *target time interval* $[T_s, T_e]$ during which the parameters of the earthquake models are
 173 estimated. One also considers a *forecasting time interval* $[T_e, T_e + \Delta T]$ during which
 174 specific measures of seismicity can be computed or evolution of seismicity can be fore-
 175 casted. For properly estimating the parameters of earthquake models, it is also impor-
 176 tant to consider the seismicity above the magnitude of completeness m_c as typical earth-
 177 quake catalogs have missing events below this magnitude.

178 For the statistical modeling of seismicity, the occurrence of earthquakes can be con-
 179 sidered as a realization of a stochastic marked point process in time (Daley & Vere-Jones,

180 2003; Vere-Jones, 2010). In this representation, the earthquakes are characterized by their
 181 occurrence times t_i and magnitudes m_i represent corresponding marks. The occurrence
 182 of earthquakes during a specified time interval can be arranged in an ordered set $\mathbf{S} =$
 183 $\{(t_i, m_i)\} : i = 1, \dots, n$. In one simplified assumption, the occurrence of earthquakes
 184 in the sequence can be described by a non-homogeneous Poisson marked point process
 185 (Utsu et al., 1995; Shcherbakov, Yakovlev, et al., 2005), where magnitudes and the time
 186 intervals between successive events are not correlated.

187 **2.2 Exponential Distribution and the Gutenberg-Richter Scaling Re-** 188 **lation**

189 The frequency-magnitude statistics of earthquake magnitudes is typically modelled
 190 by the left-truncated exponential distribution (Vere-Jones, 2010):

$$f_\theta(m) = \beta \exp[-\beta(m - m_0)], \quad (1)$$

$$F_\theta(m) = 1 - \exp[-\beta(m - m_0)], \quad \text{for } m \geq m_0, \quad (2)$$

191 where $f_\theta(m)$ is the probability density, $F_\theta(m)$ is the cumulative distribution function,
 192 and $\theta = \{\beta\}$ is the model parameter. m_0 is a given lower magnitude cutoff set above
 193 the catalog completeness level $m_0 \geq m_c$. All earthquakes above m_0 during the target
 194 time interval $[T_s, T_e]$ are used to estimate the model parameter β .

195 The parameter β is related to the b -value of the Gutenberg-Richter (GR) scaling
 196 relation, $\beta = \ln(10)b$ (Gutenberg & Richter, 1944):

$$\log_{10} N(\geq m) = a - b m, \quad (3)$$

197 where $N(\geq m)$ is the cumulative number of earthquakes above magnitude m . The GR
 198 relation combines two aspects of the occurrence of earthquakes, i.e. the frequency-magnitude
 199 statistics of earthquake magnitudes and the average rate of the occurrence of earthquakes,
 200 which is quantified through the parameter a . $N(\geq 0) = 10^a$ gives the total number of
 201 earthquakes above magnitude zero that occurred during the corresponding time inter-
 202 val.

203 The standard method to estimate the parameter β (or b -value) is to use the max-
 204 imum likelihood approach, which has an analytic solution for the point estimator of the
 205 parameter of the exponential distribution. However, in typical earthquake catalogs the
 206 magnitudes are binned and not continuous variables. Therefore, one needs to apply a

207 corrected estimator, which explicitly assumes the binning of the magnitudes (Bender,
 208 1983). For the estimation of the parameter uncertainties at a given confidence level in
 209 case of binned magnitudes one can use the method suggested in Tinti and Mulargia (1987).

210 **2.3 Omori-Utsu Law**

211 The occurrence of moderate to large earthquakes, in most cases, triggers subsequent
 212 aftershock sequences and results in the rise of seismic activity. The most accepted model
 213 that reproduces the rate of the occurrence of aftershocks is known as the Omori-Utsu (OU)
 214 law (Omori, 1894; Utsu, 1961; Utsu et al., 1995):

$$\lambda_{\omega}(t) = \frac{K_o}{(t + c_o)^{p_o}}, \quad (4)$$

215 where λ_{ω} is the rate of aftershocks per unit time for events above a certain magnitude
 216 m_0 . $\omega = \{K_o, c_o, p_o\}$ are the OU model parameters. The time t is elapsed since $T_0 =$
 217 0, which corresponds to the time of the occurrence of the mainshock. The parameter K_o
 218 describes the productivity of the sequence, c_o is a characteristic time, and p_o specifies
 219 how fast or slow the sequence decays in time. The parameters can be estimated using
 220 the maximum likelihood method and parameter uncertainties are computed using the
 221 inverse of the Fisher information matrix, which is derived from the likelihood function
 222 (Ogata, 1983, 1999). This model assumes that the occurrence of earthquakes follows a
 223 non-homogeneous Poisson process, where earthquake magnitudes are independent and
 224 identically distributed (i.i.d.) random numbers and do not influence the future earth-
 225 quake rate.

226 The Omori-Utsu law is applicable to "standard" aftershock sequences with a sin-
 227 gle mainshock and a consistently decaying rate. However, in some cases the earthquake
 228 sequence can be punctuated by several strong shocks each one of them producing their
 229 own aftershocks. In that case, a compound Omori-Utsu model can be considered (Ogata,
 230 1983; Shcherbakov et al., 2012). In a case of two strong earthquakes, it is written as:

$$\lambda_{\omega}(t) = \frac{K_1}{(t + c_1)^{p_1}} + H(t - \tau_m) \frac{K_2}{(t - \tau_m + c_2)^{p_2}}, \quad (5)$$

231 where $\omega = \{K_1, c_1, p_1, K_2, c_2, p_2\}$, time t is elapsed since the occurrence of the first
 232 event at $T_0 = 0$ and τ_m is the time of the occurrence of the second strong event. $H(x)$
 233 is a Heaviside step function and is equal to one for positive $x \geq 0$ and is zero otherwise.
 234 For the times past the occurrence of the second strong earthquake ($t \geq \tau_m$), equation (5)

235 defines the total rate as a superposition of two aftershock sequences triggered by the both
 236 strong earthquakes.

237 **2.4 Epidemic Type Aftershock Sequence (ETAS) Model.**

238 The occurrence of earthquakes is characterized by the clustering of seismicity. This
 239 clustering is a direct manifestation of the ability of earthquakes to trigger subsequent
 240 events. The ETAS model was introduced to reflect this essential aspect of the occurrence
 241 of earthquakes (Ogata, 1988, 1999, 2017). In the temporal version of the model, the con-
 242 ditional earthquake rate $\lambda_\omega(t|\mathcal{H}_t)$ at a given time t is given as (Ogata, 1988; D. Harte,
 243 2010):

$$\lambda_\omega(t|\mathcal{H}_t) = \mu + K \sum_{i:t_i < t}^{N_t} \frac{e^{\alpha(m_i - m_0)}}{\left(\frac{t-t_i}{c} + 1\right)^p}, \quad (6)$$

244 where $\omega = \{\mu, K, c, p, \alpha\}$ is a set of parameters and m_0 is a reference magnitude. The
 245 summation is performed over the history, \mathcal{H}_t , of past events up to time t during the time
 246 interval $[T_0, t]$. N_t is the number of earthquakes in the interval $[T_0, t]$ above the lower
 247 magnitude cutoff m_0 . In the ETAS process, a certain fraction of earthquakes occurs ran-
 248 domly with a constant rate μ . These earthquakes are associated with background seis-
 249 micity driven by tectonic loading and can be modelled as a homogeneous Poisson pro-
 250 cess. It is also postulated that each earthquake is capable of triggering its own offsprings.
 251 As a result, the total earthquake rate at a given time, is a superposition of the background
 252 rate given by μ and the contribution from each already occurred earthquake.

253 As the ETAS rate, equation (6), is conditioned on past seismicity \mathcal{H} , one has to
 254 minimize the effect of lack of earthquakes at the start of the sequence when estimating
 255 the ETAS parameters. For this, one can consider a short time interval $[T_0, T_s]$ before the
 256 target time interval $[T_s, T_e]$. The earthquakes in the interval $[T_0, T_s]$ can be used to prop-
 257 erly estimate the conditional earthquake rate during the target time interval $[T_s, T_e]$. The
 258 ETAS parameters $\omega = \{\mu, K, c, p, \alpha\}$ are estimated in the target time interval $[T_s, T_e]$
 259 by maximizing the likelihood function and the uncertainties are computed using the in-
 260 verse of the Fisher information matrix.

261 **2.5 Extreme Value Distribution**

262 For the sequence of earthquake that can be described as a non-homogeneous Pois-
 263 son process, the probability that the magnitude of the largest expected event will exceed

264 m for all possible number of events during a future time interval $[T_e, T_e + \Delta T]$ can be
 265 computed from the extreme value distribution (EVD) (Campbell, 1982; Coles, 2001; Da-
 266 ley & Vere-Jones, 2003):

$$P_{\text{EV}}(m_{\text{ex}} > m | \theta, \omega, \Delta T) = 1 - \exp\{-\Lambda_\omega(\Delta T) [1 - F_\theta(m)]\}, \quad (7)$$

267 where the productivity is $\Lambda_\omega(\Delta T) = \int_{T_e}^{T_e + \Delta T} \lambda_\omega(t) dt$. Using the exponential model for
 268 the magnitude distribution, equation (2), this results in the Gumbel distribution for the
 269 magnitudes of extreme earthquakes:

$$P_{\text{EV}}(m_{\text{ex}} > m | \theta, \omega, \Delta T) = 1 - \exp\{-\Lambda_\omega(\Delta T) \exp[-\beta(m - m_0)]\}. \quad (8)$$

270 Assuming that the earthquake rate is described by the OU law, equation (4), the
 271 productivity $\Lambda_\omega(\Delta T)$ can be computed explicitly and takes the following form for $p_o \neq$
 272 1:

$$\Lambda_\omega(\Delta T) = K_o \frac{(T_e + c_o)^{1-p_o} - (T_e + \Delta T + c_o)^{1-p_o}}{p_o - 1}. \quad (9)$$

273 Given a set of parameters $\{\theta, \omega\}$, which can be estimated from past seismicity during
 274 the training time interval $[T_s, T_e]$, equations (8) and (9) allow to compute the probab-
 275 ility to have the extreme earthquake above magnitude m during a future time interval ΔT .
 276 It is equivalent to the Reasenberg and Jones (1989) model.

277 For the compound OU model, equation (5), the productivity $\Lambda_\omega(\Delta T)$ can be ex-
 278 pressed as follows for $p_1 \neq 1$ and $p_2 \neq 1$:

$$\Lambda_\omega(\Delta T) = K_1 \frac{(T_e + c_1)^{1-p_1} - (T_e + \Delta T + c_1)^{1-p_1}}{p_1 - 1} + K_2 \frac{(T_e - \tau_m + c_2)^{1-p_2} - (T_e + \Delta T - \tau_m + c_2)^{1-p_2}}{p_2 - 1}, \quad (10)$$

279 where τ_m is the time of the occurrence of the second strong earthquake during the train-
 280 ing time interval $[T_s, T_e]$.

281 **2.6 Bayesian Predictive Distribution**

282 The computation of the EVD, equation (7), using specific parametric models for
 283 the earthquake rate and frequency-magnitude statistics, requires the knowledge of the
 284 model parameters. However, the true values of the model parameters are not known for
 285 specific earthquake sequences. As a result, the parameter estimates are used, which are
 286 computed with a given range of uncertainties. Those uncertainties can significantly af-
 287 fect the computation of the corresponding probabilities. The incorporation of the model

288 uncertainties into the computation of probabilities can be achieved through the Bayesian
 289 predictive distribution (BPD) (Zöller et al., 2013; Shcherbakov et al., 2018, 2019). The
 290 BPD for the largest expected event m_{ex} to be greater than a certain value m and dur-
 291 ing the forecasting time interval ΔT is:

$$P_{\text{B}}(m_{\text{ex}} > m | \mathbf{S}, \Delta T) = \int_{\Omega} \int_{\Theta} P_{\text{EV}}(m_{\text{ex}} > m | \theta, \omega, \Delta T) p(\theta, \omega | \mathbf{S}) d\theta d\omega, \quad (11)$$

292 where Θ and Ω define the multidimensional domains of the frequency-magnitude distri-
 293 bution and earthquake rate parameters, respectively. When computing the predictive
 294 distribution, equation (11), the model parameter uncertainties are fully integrated into
 295 the BPD (Renard et al., 2013; Shcherbakov et al., 2019). This is done through the use
 296 of the posterior distribution function $p(\theta, \omega | \mathbf{S})$, which characterizes the distribution of
 297 the model parameter uncertainties.

298 For the ETAS model, the extreme value distribution for the extreme events does
 299 not follow, equation (7), due to stochastic nature of the process, which deviates from a
 300 non-homogeneous Poisson process. In this case, one can compute the extreme value dis-
 301 tribution by stochastic simulation of the ETAS model and extracting the maximum mag-
 302 nitude from each simulated sequence (Shcherbakov et al., 2019).

303 To compute the BPD for a given training time interval, first, the Markov Chain
 304 Monte Carlo (MCMC) sampling of the posterior distribution is performed to generate
 305 a chain of the ETAS parameters using the Metropolis-within-Gibbs algorithm. The gen-
 306 erated chains of length N_{sim} are used to simulate the ensemble of the ETAS processes
 307 forward in time during the forecasting time interval ΔT . From each simulated sequence
 308 the maximum event is extracted and the distribution of these maxima approximates the
 309 BPD (Shcherbakov et al., 2019).

310 2.7 Forecast Validation

311 The extreme value distribution, equation (8), and the Bayesian predictive distri-
 312 bution, equation (11), allow to compute the probability of having the expected largest
 313 event during the forecasting time interval ΔT . This computation critically depends on
 314 the proper simulation of the earthquake rate and the frequency-magnitude distribution
 315 of earthquakes during ΔT . Therefore, it is important to perform specific statistical tests
 316 to validate retrospectively as to how the models, that are used to describe those aspects
 317 of seismicity, accurately reproduce the observed earthquakes during the forecasting time

318 intervals. One such test has been developed for the CSEP testing framework and is known
 319 as the N-test (Kagan & Jackson, 1995; Schorlemmer et al., 2007; Zechar et al., 2010).
 320 This test is used to quantify as to how accurately a given stochastic process reproduces
 321 the observed number of earthquakes above a certain magnitude during the forecasting
 322 time interval.

323 The following implementation of the N-test is considered in this work. It is assumed
 324 that N_{obs} earthquakes above magnitude m_0 occurred during a given forecasting time in-
 325 terval $[T_e, T_e + \Delta T]$. The posterior distribution of the parameters of a given stochas-
 326 tic point process model is sampled by the MCMC method N_{sim} times using the infor-
 327 mation of the earthquakes that occurred during the training time interval $[T_s, T_e]$. The
 328 MCMC sets of the model parameters are used to model forward in time a given point
 329 process during the forecasting time interval ΔT . The synthetic simulations produce the
 330 distribution of the number of the forecasted events at the end of the interval ΔT cor-
 331 responding to each MCMC set of model parameters. The N-test statistically assesses whether
 332 the observed number of earthquakes N_{obs} is consistent with the forecast. The two quan-
 333 tile scores are computed (Zechar et al., 2010):

$$\delta_1 = 1 - P(N_{\text{obs}} - 1 | N_{\text{fore}}) , \quad (12)$$

$$\delta_2 = P(N_{\text{obs}} | N_{\text{fore}}) , \quad (13)$$

334 where N_{fore} is the average number of forecasted events above magnitude m_0 at the end
 335 of the forecasted time interval $T_e + \Delta T$. $P(x|\lambda)$ is the cumulative Poisson distribution
 336 with the expectation λ . As a result, δ_1 gives the probability of observing at least N_{obs}
 337 events and δ_2 gives the probability of observing at most N_{obs} events. The forecast un-
 338 derpredicts the observations if δ_1 is very small and the forecast overpredicts the obser-
 339 vation if δ_2 is very small. Therefore, one can consider a one-sided test with an effective
 340 significance level α_{eff} . If the computed probabilities δ_1 and δ_2 are smaller than α_{eff} then
 341 the forecast can be rejected.

342 The second test, which is known as M-test, has been suggested to check whether
 343 the distribution of the forecasted magnitudes is consistent with the observed magnitudes
 344 (Schorlemmer et al., 2007; Zechar et al., 2010). The M-test is performed by computing
 345 a quantile score κ . The values of κ below a significance level α_{eff} signify that the distri-
 346 bution of forecasted earthquake magnitudes is inconsistent with observations. The de-
 347 tails of computing the κ score can be found in Zechar et al. (2010).

348 Two more tests have been introduced to compare the performance of different fore-
 349 casting models. These are known as R-test and T-test (Schorlemmer et al., 2007; Rhoades
 350 et al., 2011). The R-test is performed by computing the log-likelihood ratio for two mod-
 351 els under consideration. The joint log-likelihood for given earthquake observations dur-
 352 ing the forecasting time interval can be written as follows:

$$L(\mathbf{M}|\mathbf{\Lambda}) = \log [\Pr(\mathbf{M}|\mathbf{\Lambda})] = \sum_{i \in \mathbf{B}} \{-\lambda(i) + m(i) \log[\lambda(i)] - \log[m(i)!]\}, \quad (14)$$

353 where $\mathbf{M} = \{m(i)|i \in \mathbf{B}\}$ is the set of the number of earthquakes $m(i)$ in each mag-
 354 nitude bin above a certain magnitude threshold. $\mathbf{\Lambda} = \{\lambda(i)|i \in \mathbf{B}\}$ is the earthquake
 355 forecast produced by a given point process in each magnitude bin, where $\lambda(i)$ is the num-
 356 ber of earthquakes forecasted in bin i and the magnitude binning coincides with the bin-
 357 ning of the earthquake catalog. In the definition of the joint log-likelihood, equation (14),
 358 it is assumed that the number of earthquakes in a forecast bin follows a Poisson distri-
 359 bution: $\Pr(m|\lambda) = \frac{\lambda^m}{m!} \exp(-\lambda)$. To compare two models, $\mathbf{\Lambda}^1$ and $\mathbf{\Lambda}^2$, that forecast the
 360 same sequence of events one can compute the log-likelihood ratio: $R^{21} = L(\mathbf{M}|\mathbf{\Lambda}^2) -$
 361 $L(\mathbf{M}|\mathbf{\Lambda}^1)$.

362 In applying the R-test, one of the two models is assumed to be correct and is used
 363 to simulate the ensemble of synthetic earthquake events and compute the log-likelihood
 364 ratios for each synthetic record by using both models. These ratios are compared with
 365 the log-likelihood ratio computed for the observed earthquake sequence during the fore-
 366 casting interval. The properly normalized fraction of the simulated ratios that are less
 367 than the observed ratio gives the quantile score α (Schorlemmer et al., 2007). The val-
 368 ues of α that are larger than a certain significance level support the model that was as-
 369 sumed to be correct. This test is symmetric with respect to both models and can result
 370 in the situations when both models reject each other (Rhoades et al., 2011). To over-
 371 come this difficulty, a so called T-test was introduced along with the sample informa-
 372 tion gain per earthquake (Rhoades et al., 2011). The sample information gain per earth-
 373 quake of the model $\mathbf{\Lambda}^2$ over the model $\mathbf{\Lambda}^1$ is defined as $I_N(\mathbf{\Lambda}^2, \mathbf{\Lambda}^1) = R^{21}/N_{\text{obs}}$, where
 374 N_{obs} is the number of observed earthquakes during the forecasting time interval ΔT . The
 375 T-test checks whether the sample information gain is statistically different from zero that
 376 indicates a significant difference between the two models (Rhoades et al., 2011).

377 One important difference in performing the above tests is implemented in this work.
 378 To account for the stochastic variability of the model parameters and the uncertainty

379 associated with the prior information on the model parameters, the MCMC sampling
 380 of the posterior distribution of the model parameters is performed to produce a chain
 381 of model parameters that are used when simulating the models forward in time during
 382 the forecasting time interval.

383 The N-, M-, R-, and T-tests check the consistency of the underlying earthquake
 384 rate and frequency-magnitude distribution models. To test the consistency of the Bayesian
 385 predictive distribution, equation (11), with the observed largest earthquakes during the
 386 forecasting time interval $[T_e, T_e + \Delta T]$, one can evaluate the posterior predictive p -value
 387 (Gelman et al., 2013, p.146). The Bayesian p -value gives the probability that the largest
 388 simulated earthquakes can be more extreme than the observed largest earthquake dur-
 389 ing the forecasting time interval. It is defined as follows:

$$p = \Pr [T(\hat{y}, \theta, \omega) \geq T(y, \theta, \omega) | y] , \quad (15)$$

390 where $T(y, \theta, \omega)$ is a *test quantity* computed for an observed variable y and simulated
 391 variable \hat{y} . The test quantity $T(y, \theta, \omega)$ characterizes data y with given model param-
 392 eters θ and ω . It is used for model checking in Bayesian analysis similar to a test statis-
 393 tic in classical testing. One possible choice for the test quantity is: $T(y, \theta, \omega) = \max(y)$.
 394 In practice, the Bayesian p -value can be computed from the MCMC chain of the model
 395 parameters θ and ω . For each set of the model parameters, the stochastic forecasting model
 396 is simulated forward in time and the largest event is extracted. This will allow to com-
 397 pute $T(\hat{y}, \theta, \omega) = \max(\hat{y})$. The realized test quantity $T(y, \theta, \omega) = \max(y)$ is simply
 398 the value of the largest observed earthquake during the forecasting time interval. There-
 399 fore, the estimated p -value is the proportion of the test quantities for the simulated max-
 400 imum events that are larger than the observed largest event:

$$p = \frac{|\{T(\hat{y}, \theta_i, \omega_i) \geq T(y) | i = 1, \dots, N_{\text{sim}}\}|}{N_{\text{sim}}} , \quad (16)$$

401 where N_{sim} is the total number of simulated sequences from the MCMC chain and $|x|$
 402 gives the size of the set x .

403 **3 Results**

404 **3.1 Frequency-Magnitude Statistics**

405 The earthquakes within an elliptical region, given in Figure 1, were extracted dur-
 406 ing predefined target time intervals. The frequency-magnitude statistics of earthquake

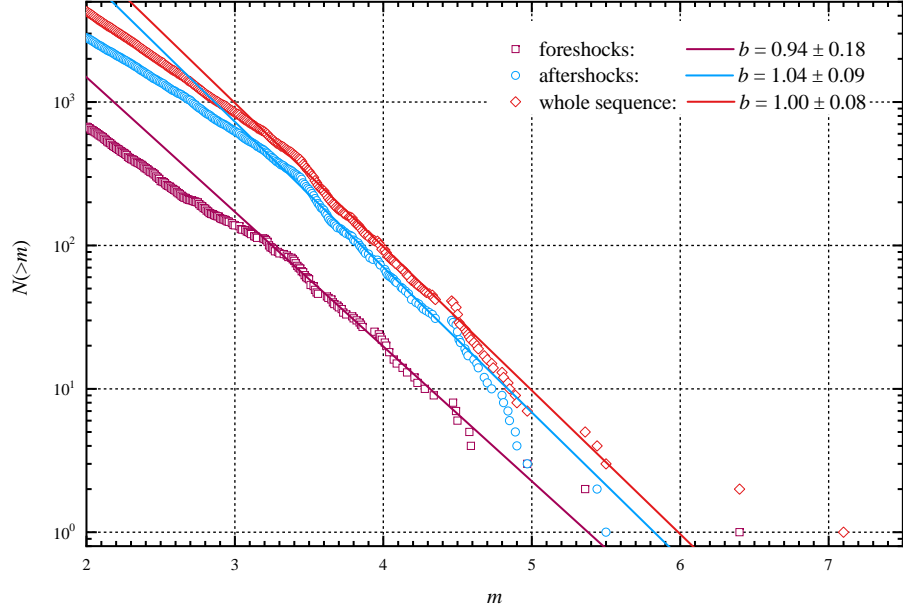


Figure 2. The frequency-magnitude statistics of earthquakes in the sequence and the modelling by the Gutenberg-Richter relation, equation (3). The symbols (representing the cumulative numbers) correspond to the foreshocks of the M7.1 mainshock (open squares), the aftershocks of the mainshock (open circles), and for the whole sequence (open diamonds). The fits of the GR relation are plotted as straight lines. The estimated b -values are given in the legend for all earthquakes above $m \geq 3.2$. The uncertainties are given as 95% confidence intervals.

407 magnitudes were computed for the foreshock sequence starting from 2019/07/04 (17:02:55
 408 UTC) which corresponds to $T_0 = 0$ and during 1.428 days with $[T_s, T_e] = [10^{-5}, 1.428]$.
 409 It was also computed for the aftershocks of the M7.1 mainshock starting from 2019/07/06
 410 (03:19:53 UTC) during 7 days after the mainshock. The frequency-magnitude statistics
 411 was also computed for the whole sequence including both foreshocks and aftershocks dur-
 412 ing 31 days. The results are given in Figure 2 as open symbols for events larger than $m \geq$
 413 2.0. The maximum likelihood fits of the exponential distribution, equation (1), to the
 414 frequency-magnitude data is also shown as GR plots with estimated b -values using the
 415 method of Bender (1983) and their 95% confidence intervals according to Tinti and Mu-
 416 largia (1987).

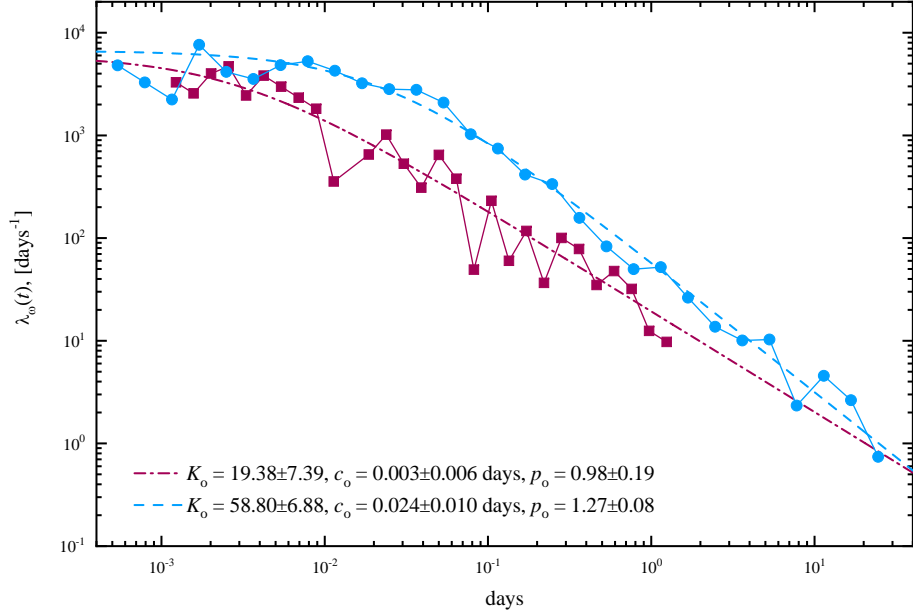


Figure 3. The earthquake decay rates for the foreshock sequence (solid squares) and for the aftershock sequence (solid circles). The corresponding fits of the Omori-Utsu law, equation (4), to the foreshock (dash-dotted line) and aftershock (dashed line) sequences. The estimated parameters with the corresponding 95% confidence intervals are given in the legend using all earthquakes above magnitude $m \geq 3.2$.

417 3.2 Earthquake Rate Evolution and Modelling

418 First, the earthquake rate was modelled separately for the foreshock and aftershock
 419 sequences using the OU law, equation (4). The results are given in Figure 3 for all earth-
 420 quakes above magnitude $m \geq 3.2$. For the foreshock sequence, the following target time
 421 interval was used $[T_s, T_e] = [10^{-3}, 1.428]$ with $T_0 = 0$ corresponding to 2019/07/04
 422 (17:33:49 UTC). For the aftershock sequence, $T_0 = 0$ was set to the occurrence of the
 423 M7.1 mainshock on 2019/07/06 (03:19:53 UTC) with the target time interval $[T_s, T_e] =$
 424 $[10^{-3}, 30]$ days. The OU law parameters for the foreshock and aftershock sequences are
 425 given in the legend with the corresponding 95% confidence intervals.

426 Next, the compound OU model, equation (5), was used to fit the sequence start-
 427 ing from the occurrence of the M6.4 foreshock on 2019/07/04 (17:33:49 UTC) correspond-
 428 ing to $T_0 = 0$ and during the following target time interval $[T_s, T_e] = [10^{-3}, 8.407]$
 429 days. All earthquakes above magnitude $m \geq 3.2$ were considered. This is illustrated

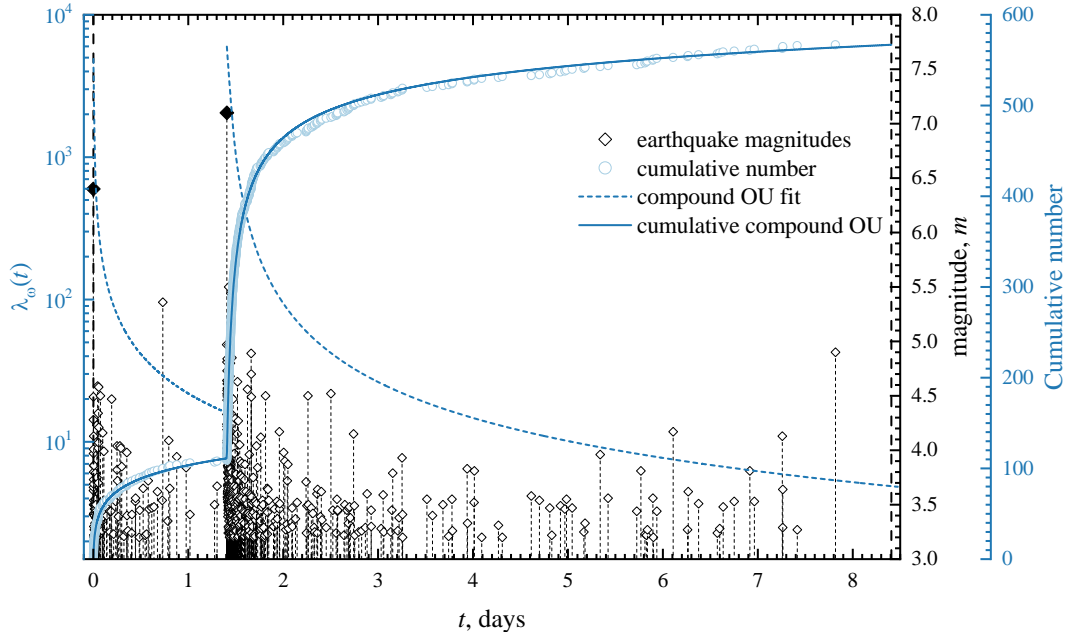


Figure 4. The occurrence of earthquakes during the evolution of the 2019 Ridgecrest sequence and the fitting of the compound Omori-Utsu law, equation (5). $T_0 = 0$ corresponds to the occurrence of M6.4 foreshock on 2019/07/04 (17:33:49 UTC). The earthquake magnitudes are plotted as open diamond symbols. The cumulative number of earthquakes is plotted as open circles. The dashed curve corresponds to the fit of the compound Omori-Utsu law, equation (5). The corresponding fit of the cumulative numbers is given as a solid curve. All earthquakes above magnitude $m \geq 3.2$ were used.

430 in Figure 4 and Figure S1. The maximum likelihood fitting of the compound OU model
 431 yielded the following parameters $\{K_1, c_1, p_1, K_2, c_2, p_2\} = \{21.92, 0.0019, 0.92, 40.14, 0.043, 1.59\}$.

432 The ETAS model was fitted to the 2019 Ridgecrest sequence using a number of tar-
 433 get time intervals for all the events above magnitude $m \geq 3.2$. In one particular exam-
 434 ple, the training time interval $[T_s, T_e] = [0.03, 7.428]$ days was used with $T_0 = 0.0$ cor-
 435 responding to the start date 2019/07/04 (17:02:55 UTC). The estimated conditional rate,
 436 equation (6), and the corresponding earthquake magnitudes above the lower threshold
 437 $m \geq 3.2$ are plotted in Figure 5 and Figure S2. For comparison, the separate fits of the
 438 Omori-Utsu law to the foreshocks and aftershocks of the M7.1 mainshock are also plot-
 439 ted with the parameters given in Figure 3.

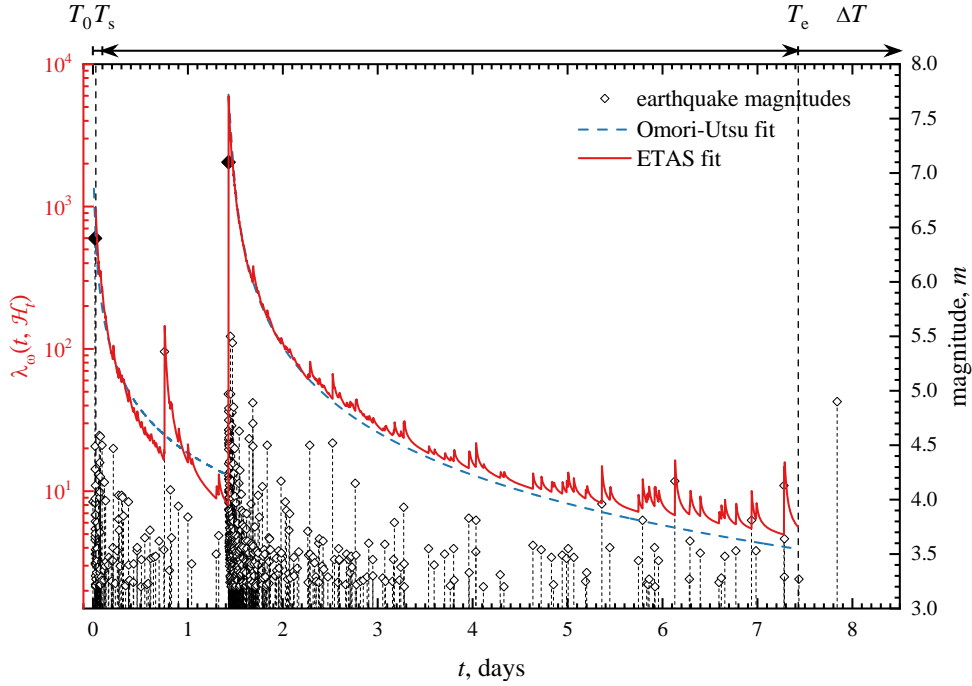


Figure 5. The occurrence of earthquakes during the evolution of the 2019 Ridgecrest sequence and the fitting of the ETAS model, equation (6). The start of the sequence $T_0 = 0$ corresponds to the time of the occurrence of the M3.98 foreshock on 2019/07/04 (17:02:55 UTC). All the events above magnitude $m \geq 3.2$ are shown. The ETAS model is fitted to the sequence during the target time interval $[T_s, T_e] = [0.03, 7.428]$ days. The estimated conditional earthquake rate (solid curve) is plotted using the following ETAS parameters: $\mu = 0.05$, $K = 1.255$, $c = 0.023$, $p = 1.39$, and $\alpha = 2.18$. For comparison, the Omori-Utsu law fit, equation (4), is plotted as a short-dashed curve.

440 Finally, the point estimates of the model parameters and their 95% confidence in-
 441 tervals were computed at predefined times during the evolution of the sequence. This
 442 is illustrated in Figure 6. The reported b -value at time 1.428 days corresponds to the fore-
 443 shock sequence starting from the occurrence of the M3.98 foreshock on 2019/07/04 (17:02:55
 444 UTC). The frequency-magnitude statistics and the fitting of the GR relation to the fore-
 445 shock sequence is also illustrated in Figure 2. The subsequent estimates of b -values at
 446 days 1d, 2d, etc., correspond to the time duration of the aftershock sequence since the
 447 M7.1 mainshock (Figure 6a). Similarly, the parameters of the OU law, equation (4), were
 448 estimated during the same time intervals (Figure 6b). In addition, the point estimates
 449 of the ETAS model parameters were also computed. This is given in Figure 6c. The pa-
 450 rameter μ was held constant at $\mu = 0.05$ to improve the stability of the parameter es-
 451 timation. It was assumed that the background seismicity rate for earthquakes above mag-
 452 nitude $m \geq 3.2$ was relatively low in this region prior to the start of the sequence.

453 3.3 Forecasting the Magnitude of the Largest Expected Earthquake

454 The EVD, equation (7), and the BPD, equation (11), were used to compute ret-
 455 rospectively the probabilities of having the largest expected earthquakes to occur dur-
 456 ing predefined times of the evolution of the 2019 Ridgecrest earthquake sequence. This
 457 was done both before and after the occurrence of the M7.1 mainshock using the OU, equa-
 458 tion (4), compound OU, equation (5), or ETAS, equation (6), parametric models for the
 459 earthquake rate and the exponential distribution, equation (2), for the distribution of
 460 earthquake magnitudes. When computing the probabilities for the aftershock sequence
 461 generated by the M7.1 mainshock two cases were analyzed. In the first consideration,
 462 only the aftershocks were used. However, when using the ETAS model and the compound
 463 OU model the foreshock sequence was also incorporated into the analysis.

464 First, the only aftershocks of the M7.1 mainshock were used to compute the prob-
 465 abilities of having the strongest aftershocks above a specified magnitude during a future
 466 time interval of $\Delta T = 7$ days. The occurrence of the M7.1 mainshock on 2019/07/06
 467 (03:19:53 UTC) corresponded to $T_0 = 0$ with the target time interval $[T_s, T_e] = [10^{-4}, 1.0]$.
 468 One particular example is given in Figure 7, where the EVD, equation (8), was computed
 469 after 1 day for all aftershocks above magnitude $m \geq 3.2$ and plotted as a short dashed
 470 curve. The following model parameter estimates were used: $\beta = 2.18$ and $\{K_o, c_o, p_o\} =$

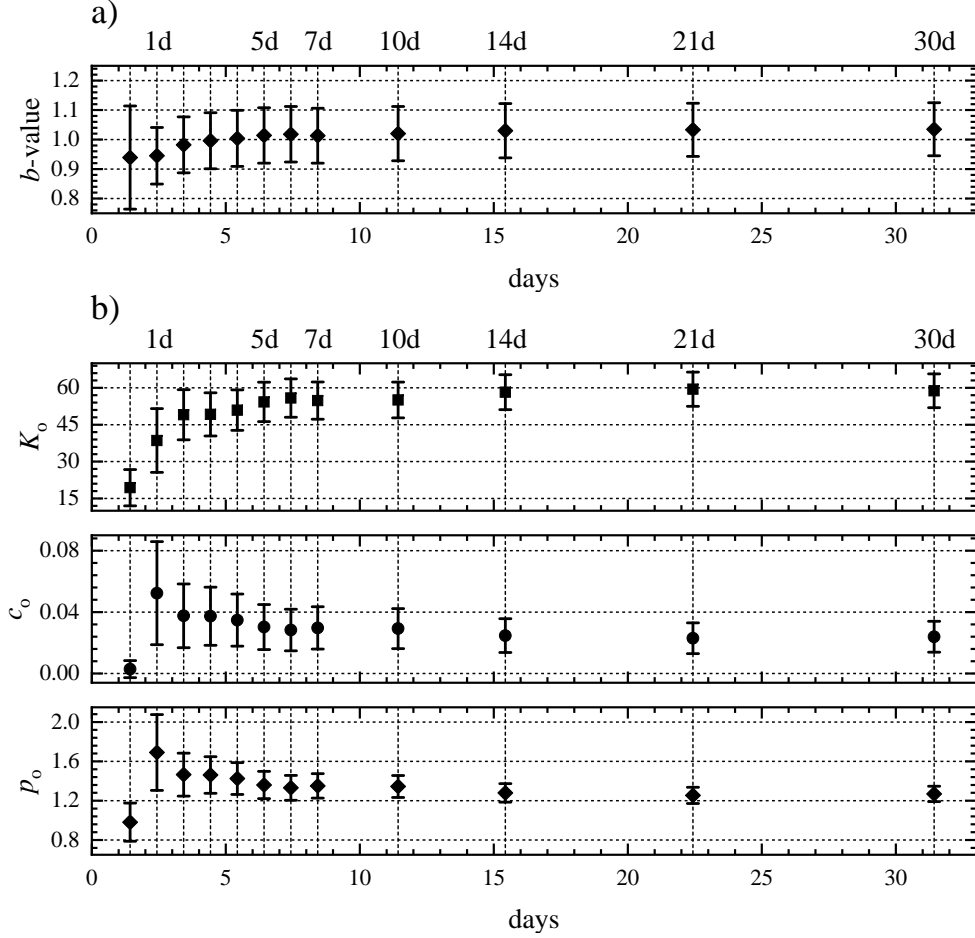


Figure 6. Point estimates of the model parameters during the evolution of the 2019 Ridgecrest sequence. The start of the sequence $T_0 = 0$ corresponds to the time of the occurrence of the M3.98 foreshock on 2019/07/04 (17:02:55 UTC). All the events above magnitude $m \geq 3.2$ were used to compute the parameters using the maximum likelihood method. The point estimates of a) the b -value; b) the Omori-Utsu parameters, equation (4), and c) the ETAS parameters, equation (6), are plotted. The 95% confidence intervals are also given. The vertical dashed lines correspond to the times in days since the occurrence of the M7.1 mainshock.

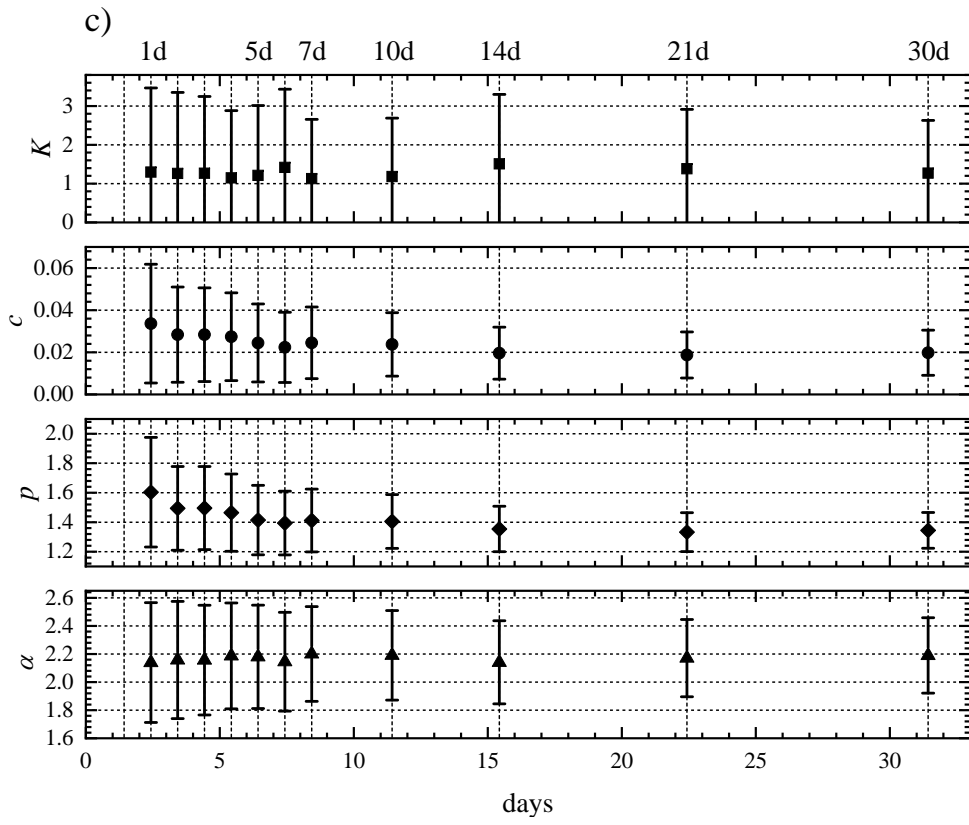


Figure 6. Continued.

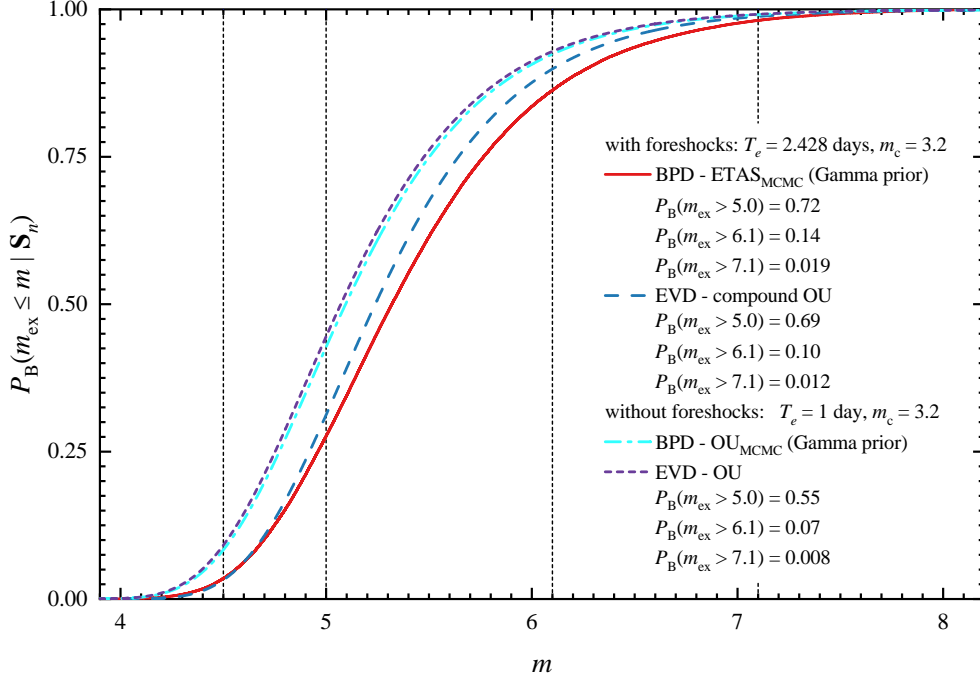


Figure 7. The extreme value and the Bayesian predictive distributions for the 2019 Ridgecrest sequence. The BPD is shown as a solid curve using the ETAS model and MCMC sampling with the Gamma prior for the foreshocks and 1 day of aftershocks after the M7.1 mainshock. For the same sequence of events, the EVD using the compound OU law is shown as a dashed curve. For the rest of the distributions, 1 day of aftershocks after the M7.1 mainshock was used: the OU rate using the MCMC sampling with the Gamma prior (short dashed curve); the Gumbel distribution with OU rate (dash-dotted curve).

471 $\{38.57, 0.052, 1.691\}$. The corresponding probabilities to have strong aftershocks above
 472 $m_{\text{ex}} \geq 5.0, 6.1, 7.1$ are also given.

473 Next, the BPD, equation (11), was computed using the aftershocks of the M7.1 main-
 474 shock during different training time intervals to forecast the magnitudes of the largest
 475 expected earthquakes to occur during the evolution of the sequence. The OU law, equa-
 476 tion (4), was used to approximate the earthquake rate. The exponential distribution, equa-
 477 tion (2), was used to model the frequency-magnitude statistics. The forecasting time in-
 478 terval was fixed at $\Delta T = 7$ days. The computed BPD to estimate probabilities for the
 479 largest expected aftershocks above magnitude $m \geq 3.2$ during one day after the main-
 480 shock is plotted in Figure 7 as a dash-dotted curve. This was done by employing the MCMC
 481 sampling of the posterior distribution and the Gamma distribution for the priors of the

482 model parameters (Shcherbakov et al., 2019). The total number of 150,000 MCMC sam-
 483 pling steps were performed for each model. The first 50,000 steps were discarded as "burn
 484 in" and the remaining $N_{\text{sim}} = 100,000$ sampling steps were used for the synthetic model
 485 simulations or analysis. For the OU model, this is given in Figure S3. The distribution
 486 of the OU model parameters computed from the MCMC chain is illustrated in Figure S4.
 487 The matrix plot of the pairs of the OU model parameters is given in Figure S5. The val-
 488 ues for the mean and variance of the prior distribution (Gamma) of the OU model pa-
 489 rameters are provided in Table S1.

490 To investigate the influence of the foreshocks on the computation of the probabilit-
 491 ities for the largest expected aftershocks, the EVD, equation (8), using the compound
 492 OU law, equation (5), and the BPD using the ETAS model, equation (6), were computed
 493 for the earthquake sequence starting from the occurrence of the first M3.98 foreshock
 494 on 2019/07/04 (17:02:55 UTC). The earthquakes above magnitude $m \geq 3.2$ were used.
 495 In case of the BPD with the ETAS model, the target time interval $[T_s, T_e] = [0.03, 2.408]$
 496 days was used with $T_0 = 0$ corresponding to 2019/07/04 (17:02:55 UTC), which included
 497 the foreshocks and one day of aftershocks after the M7.1 mainshock. The values for the
 498 mean and variance of the prior distribution (Gamma) of the compound OU and ETAS
 499 model parameters are provided in Tables S2-S3. The resulting BPD is plotted as a solid
 500 curve in Figure 7. The probabilities of having the largest expected earthquakes during
 501 the next $\Delta T = 7$ days are provided in the legend. For the same sequence, the EVD,
 502 equation (8), with the compound OU law, equation (10), was computed and the corre-
 503 sponding probabilities to have the largest aftershocks during the next $\Delta T = 7$ days were
 504 estimated. This is plotted as a dashed curve in Figure 7. The MCMC sampling steps
 505 are given in Figure S6. The distribution of the compound OU model parameters com-
 506 puted from the MCMC chain is illustrated in Figure S7. The matrix plot of the pairs
 507 of the compound OU model parameters is given in Figure S8.

508 The probabilities to have the largest expected earthquake above a certain magni-
 509 tude can be computed at specified times during the evolution of the sequence. This can
 510 be done by increasing progressively the upper limit T_e of the target time interval $[T_s, T_e]$
 511 for a fixed forecasting interval ΔT . Figure 8 illustrates the computed probabilities from
 512 the BPD, equation (11), with the ETAS model, equation (6), as an earthquake rate, and
 513 the exponential distribution, equations (2), for the frequency-magnitude statistics. $T_0 =$
 514 0 corresponded to the date 2019/07/04 (17:02:55 UTC) and $T_s = 0.03$ days. The MCMC

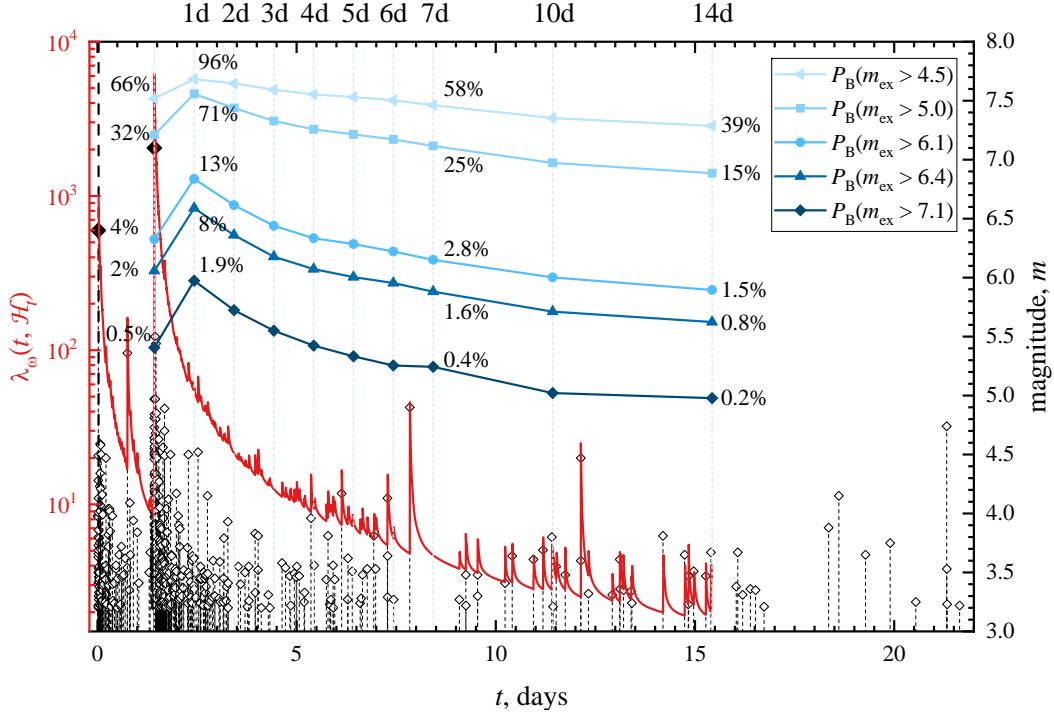


Figure 8. The probabilities for the largest expected earthquake to be above the magnitudes $m_{ex} \geq 4.5, 5.0, 6.1, 6.4, 7.1$ and during the progressively increasing time intervals since 2019/07/04 (17:02:55 UTC). The probabilities are estimated using the BPD combined with the ETAS model for the earthquake rate during the forecasting time interval $\Delta T = 7$ days and plotted in a logarithmic scale. The earthquake magnitudes of the 2019 Ridgecrest sequence are plotted as open diamonds for all events above magnitude $m \geq 3.2$. The fit of the ETAS model is shown as a solid curve.

515 sampling steps, the distribution of the ETAS model parameters, and the matrix plot of
 516 the pairs of the ETAS parameters are given in Figures S9-S11. The probabilities were
 517 estimated for the largest expected earthquakes to be larger than $m_{ex} \geq 5.0, 6.1, 6.4,$
 518 and 7.1. First, the probabilities were computed using only the foreshock sequence right
 519 before the occurrence of the M7.1 mainshock with $T_e = 1.4284$ days. After that, the
 520 probabilities were recomputed for each subsequent day after the M7.1 mainshock by in-
 521 corporating the information from the newly occurred aftershocks. For reference, the fit
 522 of the ETAS model is also shown as a red curve using the following estimated model pa-
 523 rameters $\{\beta, \mu, K, c, p, \alpha\} = \{2.3, 0.05, 1.51, 0.02, 1.35, 2.14\}$ during the training time
 524 interval $[T_s, T_e] = [0.03, 15.4284]$ days.

Finally, Figure 9 provides a comparison of the results for the computation of the probabilities to have the expected largest aftershock to be greater than $m_{\text{ex}} \geq 6.1$ after progressively increasing times T_e during the evolution of the sequence by using several methods examined in this work. The forecasting time interval was set to $\Delta T = 7$ days and all the earthquakes above magnitude $m \geq 3.2$ were considered. Specifically, the EVD with the OU law, equations (8) and (9), was used and the estimated probabilities are plotted as solid squares. Next, the compound OU law, equation (10), was used in the EVD computation and the results are plotted as solid circles in Figure 9. The computed probabilities from the BPD, equation (11), with the ETAS model, equation (6), as the earthquake rate are plotted as solid triangles. And finally, the probabilities were computed from the BPD with the earthquake rate modelled using the standard OU law, equation (4) and are plotted as solid diamonds.

3.4 Model and Forecast Validation

The three point process models (OU, compound OU, and ETAS) were examined to see whether they were consistent with the observed seismicity during the forecasting time intervals $[T_e, T_e + \Delta T]$. For this, N- and M-tests were performed. Figure 10a shows the observed number of earthquakes above magnitude $m \geq 3.2$ (as solid black diamonds) during a fixed forecasting time interval $\Delta T = 7$ days and varying training time interval $[T_s, T_e]$. The numbers are plotted at the end of the forecasting time interval with the training interval ending after 1, 2, 3, 4, 5, 6, 7, 10, 14, 30 days after the M7.1 mainshock (the corresponding $T_e = 2.4284, 3.4284, \dots, 11.4284, 15.4284, 31.4284$). For example, the first symbol at $T_e + \Delta T = 9.4284$ days gives 86 earthquakes above magnitude 3.2 that occurred during 7 days starting after 1 day ($T_e = 2.4284$) after the M7.1 mainshock. It also shows the average forecasted numbers of earthquakes with the corresponding 95% bands (plotted as shaded regions) simulated by the three models. Each model was simulated $N_{\text{sim}} = 100,000$ times forward in time during $\Delta T = 7$ days and for the varying ends of the training time interval T_e . For each model simulation, the parameters were chosen from the MCMC chain obtained by sampling the posterior distribution of the model parameters. This allowed to incorporate the variability of the model parameters into the forecasted numbers. Similarly, Figure 10b illustrates the observed and forecasted number of earthquakes when the end of the training time interval was held fixed at $T_e = 3.4284$ days (2 days after the M7.1 mainshock) and the forecasting time

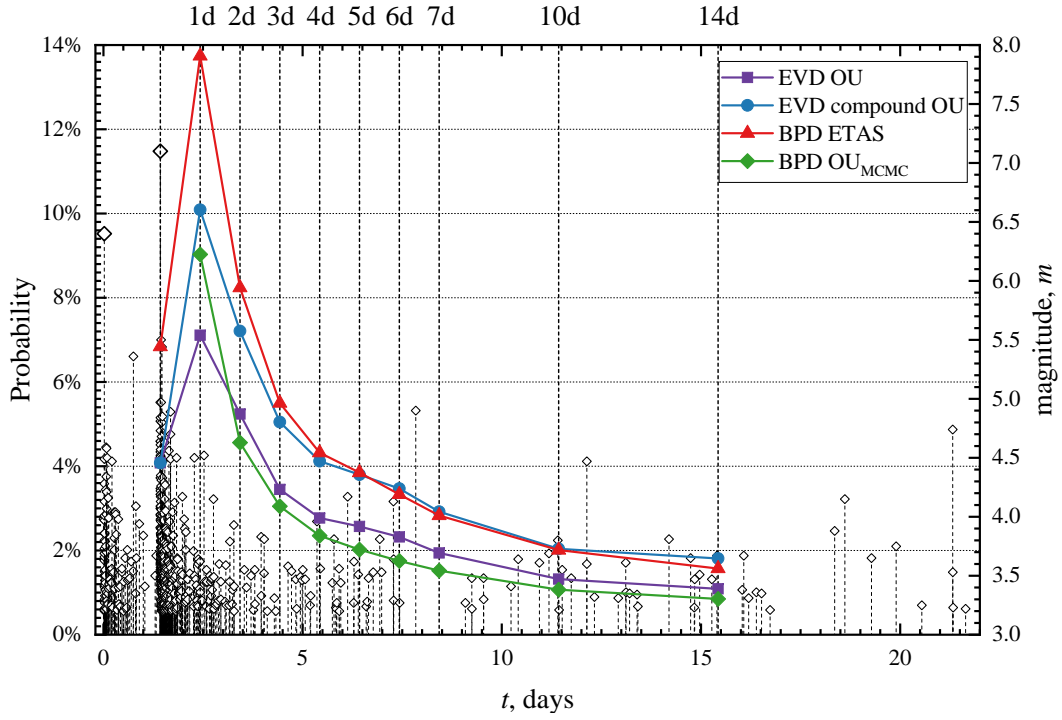


Figure 9. The comparison of the computed probabilities for the largest expected after-shock to be above magnitude $m_{\text{ex}} \geq 6.1$ during the progressively increasing time intervals since 2019/07/04 (17:02:55 UTC) for the fixed forecasting time interval $\Delta T = 7$ days. The four models were considered: the EVD with the OU law (solid squares), the EVD with the compound OU formula (solid circles), the BPD with the ETAS model (solid triangles), and the BPD with the OU law (solid diamonds). The earthquake magnitudes of the 2019 Ridgecrest sequence are plotted as open diamonds for all events above magnitude $m \geq 3.2$.

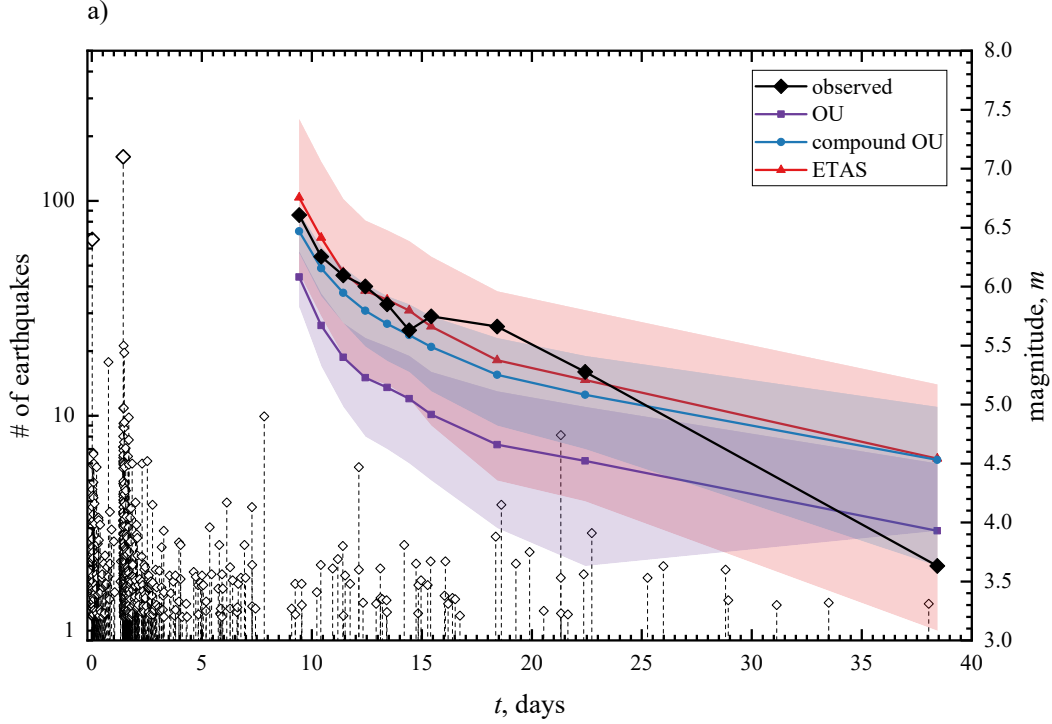


Figure 10. The observed and forecasted numbers of earthquakes starting after one day of aftershocks post M7.1 mainshock and during specified forecasting and training time intervals by using the three rate models: Omori-Utsu (OU), compound OU, and ETAS. a) The forecasting time interval $\Delta T = 7$ days is fixed while the end of the training time interval T_e is progressively increasing as $T_e = 2.428, 3.428, \dots, 15.428, 31.428$ days. The symbols indicate the number of the observed (black solid diamonds) and the mean number of forecasted earthquakes during $\Delta T = 7$ days computed at times $T_e + \Delta T$. b) The end of the training time interval is fixed at $T_e = 3.428$ days while the forecasting time interval is increasing as $\Delta T = 1, 2, 5, 7, 10, 14$. The shaded bands correspond to 95% confidence intervals.

557 interval varied $\Delta T = 1, 2, 5, 7, 10, 14$ days. For the compound OU and ETAS mod-
 558 els the preceding foreshock sequence was used. For the OU model only the aftershocks
 559 of the M7.1 mainshock were used.

560 To analyze to what extent the considered models underpredicted or overpredicted
 561 the observed sequence of earthquakes, the N-test was performed. The quantile scores com-
 562 puted during the N-test corresponding to the forecasting of the number of earthquakes
 563 are illustrated in Figure 11ab. Two threshold quantiles are plotted at 0.025 and 0.05 lev-
 564 els. δ_1 and δ_2 scores, Equations (12) and (13), were computed and plotted for the three

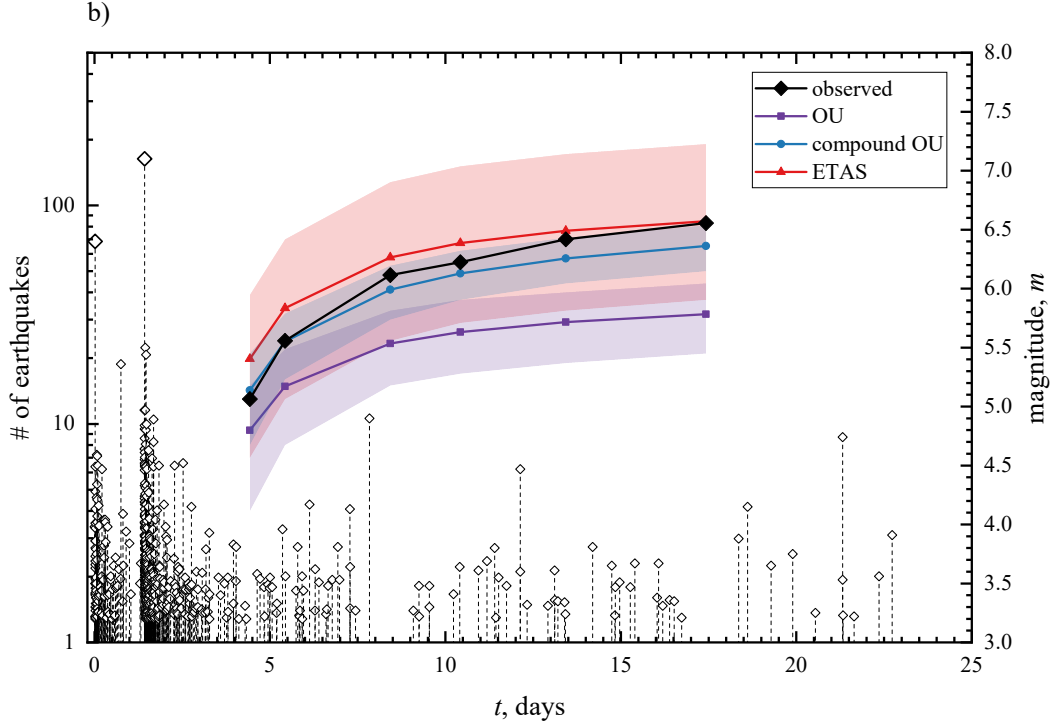


Figure 10. Continued.

565 models for the same forecasting time intervals of duration $\Delta T = 7$ days as used in Fig-
 566 ure 10a. In addition, the results of the M-test for the three models and for the same fore-
 567 casting time intervals are plotted in Figure 11c, where the quantile score κ character-
 568 izes the consistency of the forecasted earthquake magnitudes compared to the observed
 569 ones in each forecasting time interval. The quantile scores in a case of the varying fore-
 570 casting time interval $\Delta T = 1, 2, 5, 7, 10, 14$ days and fixed training time interval $T_e =$
 571 3.4284 days are given in Figure S12.

572 The models were also compared among each other by applying the R- and T-tests.
 573 Two pairs of the models were considered, i.e. the forecasts produced by the ETAS model
 574 versus the model with the OU law and the ETAS model versus the model with the com-
 575 pound OU law. The results of the quantile score α for the R-test are plotted in Figure 12.
 576 The scores α were computed at the end of each forecasting time interval of duration ΔT
 577 as in Figure 10a. The corresponding sample information gain $I_N(\mathbf{\Lambda}^2, \mathbf{\Lambda}^1)$ for each pair
 578 of the models is illustrated in Figure 13. The quantile score α and the information gain
 579 per earthquake in a case of the varying forecasting time interval $\Delta T = 1, 2, 5, 7, 10, 14$
 580 days and fixed training time interval $T_e = 3.4284$ days are given in Figures S13 and S14.

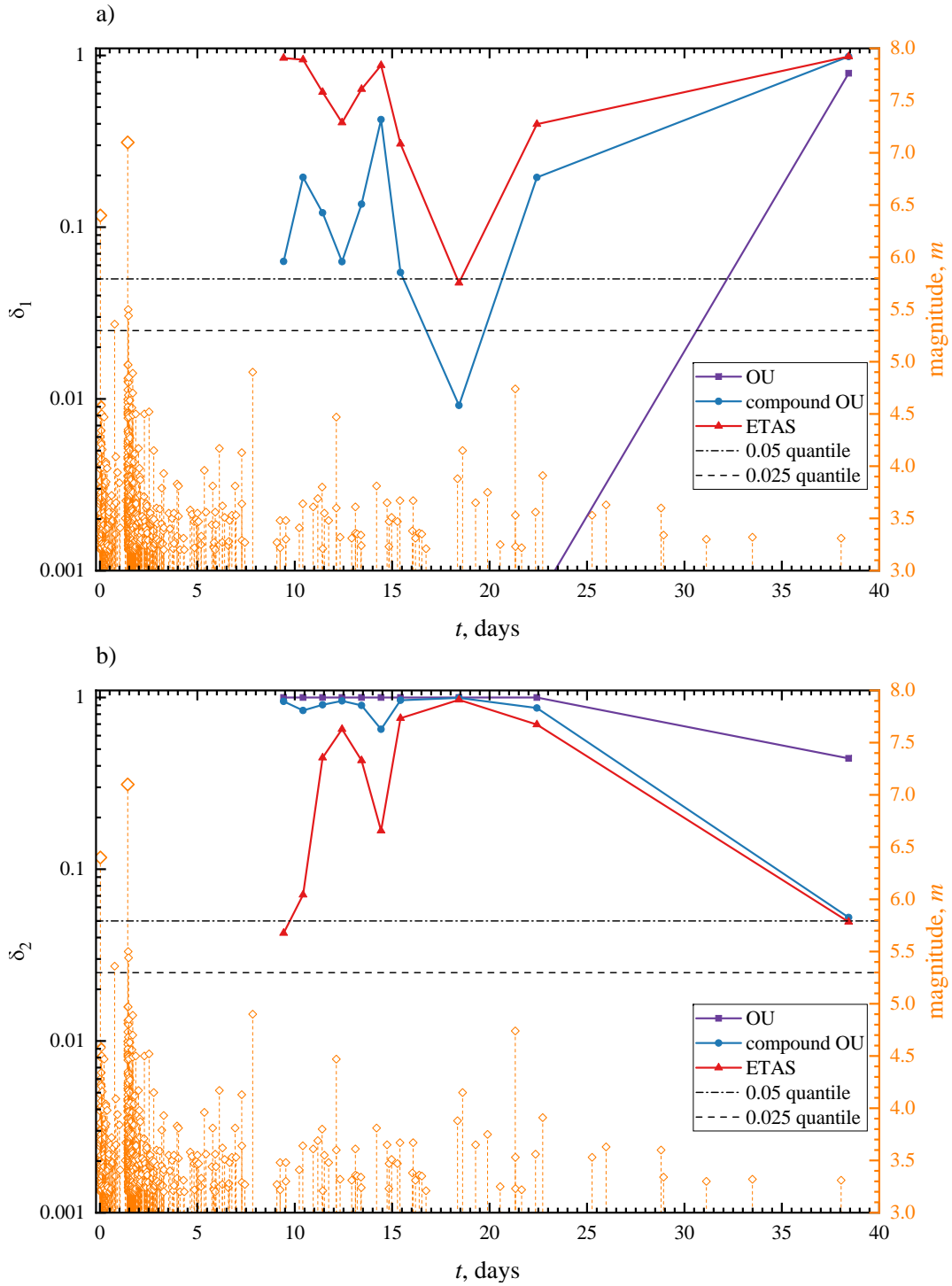


Figure 11. Plot of the quantile scores a) δ_1 (N-test), b) δ_2 (N-test), and c) κ (M-test) for the performance of the aftershock forecasts based on the three point process models. The scores are computed at the end of each forecasting time interval of fixed duration $\Delta T = 7$ days and varying training time intervals $[T_s, T_e]$ as in Figure 10.

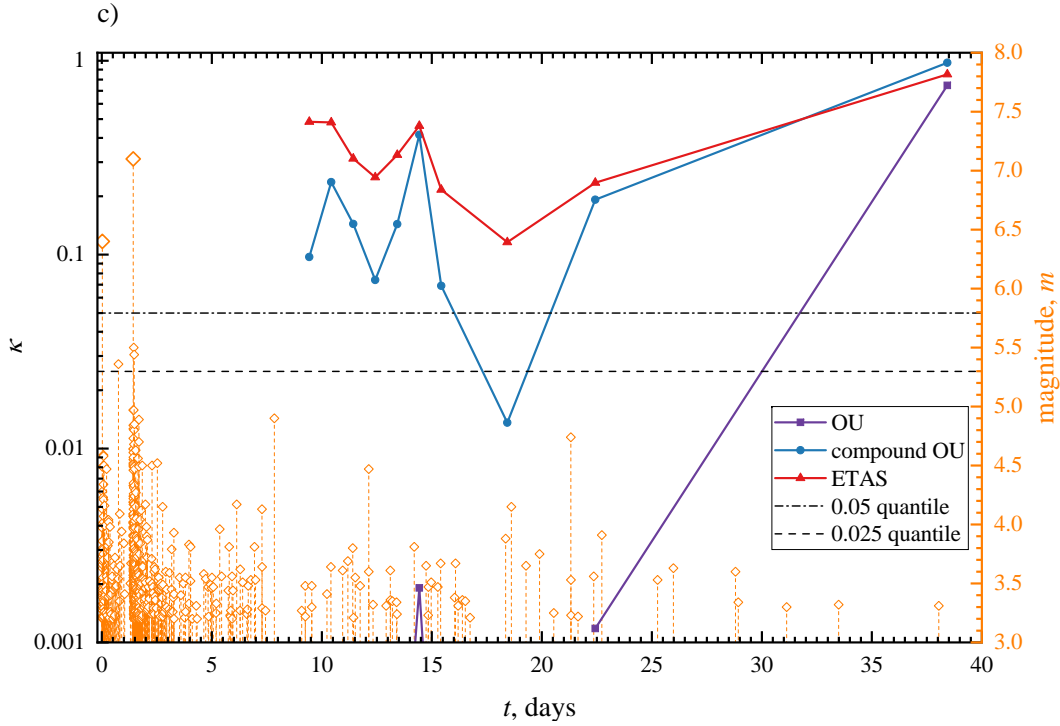


Figure 11. Continued.

581 In both pairs of models, it was assumed that the ETAS model (with the forecast Λ^2) is
 582 the correct model to simulate the synthetic sequences of events during the forecasting
 583 time intervals.

584 Finally, the Bayesian p -values, equation (16), were computed for the three mod-
 585 els. This is plotted in Figure 14 for the varying training time intervals. Figure S15 il-
 586 lustrates the dependency of the p -value on the varying forecasting time interval as in Fig-
 587 ure S13.

588 4 Discussion

589 The 2019 Ridgecrest earthquake sequence occurred in a complex network of fault
 590 structures. It generated a prominent foreshock sequence that culminated in the occur-
 591 rence of the M7.1 mainshock, which was followed by a productive aftershock sequence.
 592 This complexity of the sequence was partially reflected in the frequency-magnitude statis-
 593 tics of foreshocks and aftershocks. It also manifested in the clustering of earthquakes in
 594 time and in space. The complex pattern of multi-segmented ruptures of the two strongest

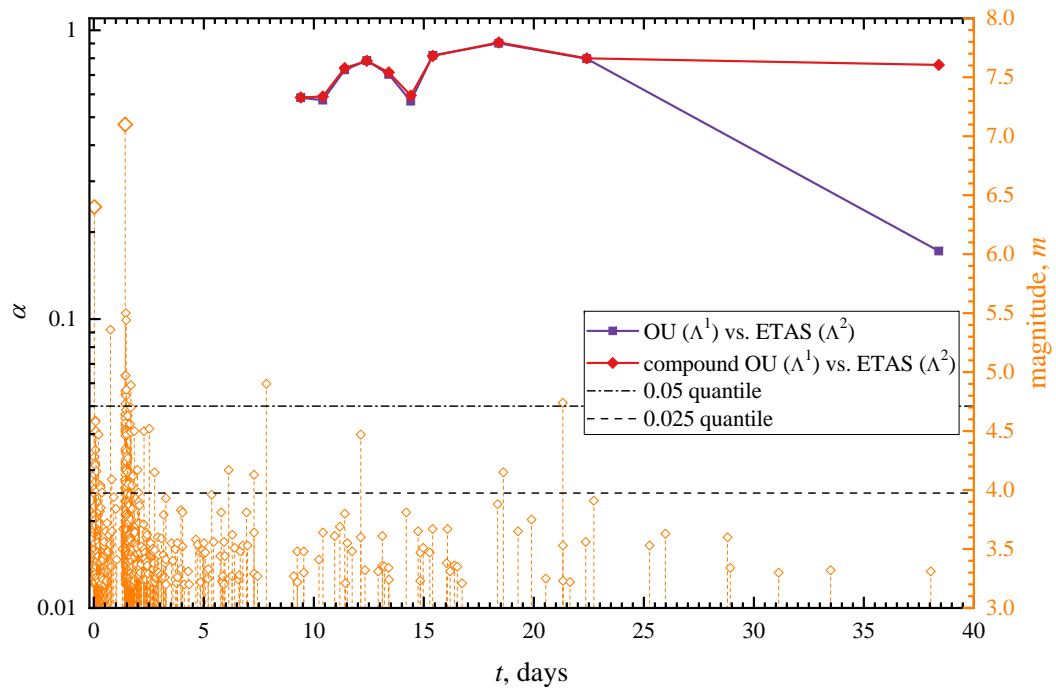


Figure 12. Plot of the quantile score α (R-test) for the comparative test of the ETAS model versus the forecast based on the OU model and on the compound OU model. The scores are computed at the end of each forecasting time interval as in Figure 11.

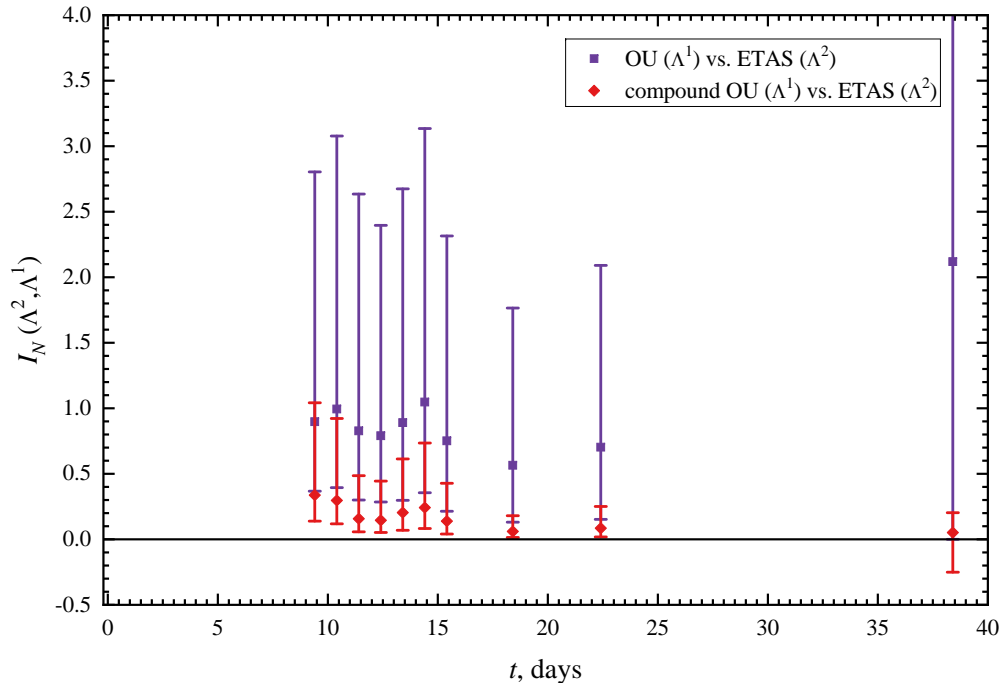


Figure 13. The sample information gain for the pairs of the models. The solid squares correspond to the comparison of the forecasts based on the ETAS model versus the forecasts based on the OU model. The solid diamonds correspond to the comparison of the forecasts based on the ETAS model versus the forecast based on the compound OU model. The 95% confidence intervals are given.

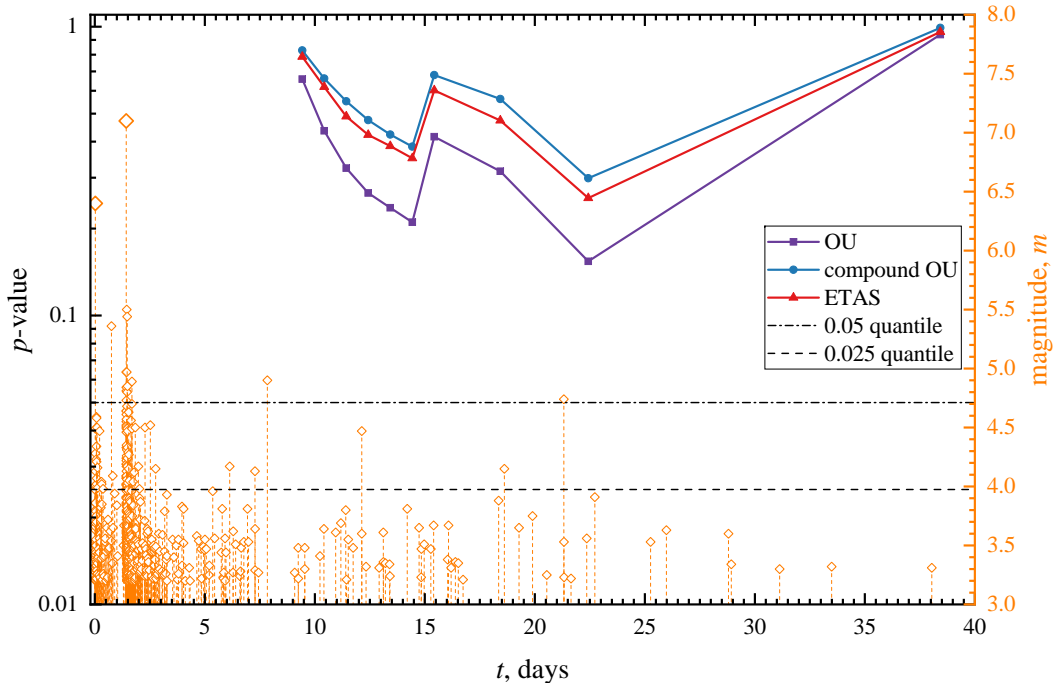


Figure 14. Plot of the Bayesian predictive distribution p -value for the three models. The p -values are computed at the end of each forecasting time interval as in Figure 11.

595 events in the sequence contributed to the assumed stress transfer pattern, which affected
 596 the distribution of subsequent triggered aftershocks.

597 The sequence exhibited a change in the slope of the frequency-magnitude statis-
 598 tics around a magnitude 3.2. This was the reason to use only the events above this value
 599 in the analysis. This change in the behavior can be the result of the early aftershock in-
 600 completeness observed right after the M6.4 foreshock and the M7.1 mainshock or it can
 601 be related to the fact that the aftershocks occurred on a distributed fault network and
 602 the geometrical distribution of fault sizes affected the statistics of earthquake magnitudes.
 603 The fit of the exponential distribution, equation (2), (or the corresponding Gutenberg-
 604 Richter relation) to the frequency-magnitude statistics of the foreshock and aftershock
 605 sequences with magnitudes above $m \geq 3.2$ produced the b -values which were typical
 606 for tectonic earthquakes as illustrated in Figure 2. The largest aftershock of the M7.1
 607 mainshock had a magnitude 5.5 and occurred less than half an hour after the mainshock.
 608 Two more strong aftershocks of magnitude 4.7 and 5.0 occurred later in the sequence
 609 on 20th and 48th days after the mainshock. The value of the largest occurred aftershock

610 is lower than what would be expected from Båth's law (Båth, 1965). It is possible that
 611 the M6.4 foreshock partially released the accumulated strain energy in the region and
 612 this resulted in a lower magnitude of the largest occurred aftershock.

613 The earthquake decay rates after the M6.4 foreshock and M7.1 mainshock exhib-
 614 ited a consistent pattern observed in other prominent aftershock sequences. The fit of
 615 the OU law, equation (4), produced $p = 1.03 \pm 0.14$ for the foreshock sequence and $p =$
 616 1.27 ± 0.04 for the aftershock sequence as illustrated in Figure 3. The smaller p -value
 617 for the foreshock sequence can be the result of a strong M5.36 foreshock that occurred
 618 16.2 hours before the M7.1 mainshock and triggered its own sequence of events. The in-
 619 fluence of the foreshock sequence on the overall rate of aftershocks was incorporated by
 620 employing the compound OU law, equation (5), or the ETAS process, equation (6), to
 621 model the earthquake decay rate (Figure 4).

622 One of the main objectives of this work was to provide a framework to compute
 623 the probabilities for the occurrence of the largest expected aftershocks during different
 624 stages of the evolution of this earthquake sequence by incorporating the preceding seis-
 625 micity. This was accomplished through two main approaches. The first one was based
 626 on the assumption that the occurrence of earthquakes could be modelled as a non-homogenous
 627 Poisson process with a specified parametric model for the earthquake rate and the frequency-
 628 magnitude distribution. Specifically, one can use the OU law, equation (4), or the com-
 629 pound OU law, equation (5), and the exponential distribution for the earthquake mag-
 630 nitudes, equation (2). Then, the probabilities can be estimated from the EVD, equation (8),
 631 for a specific forecasting time interval ΔT by using the point estimates of the model pa-
 632 rameters. The second approach employed the computation of the BPD, equation (11),
 633 which allowed to incorporate the uncertainties of the model parameters into the com-
 634 putation of the BPD. This approach also requires to provide certain *a priori* knowledge
 635 on the model parameters specified through the prior distributions.

636 The comparison of these two approaches with the combination of the three mod-
 637 els for the earthquake rate and either including or excluding the foreshocks is illustrated
 638 in Figure 7. The results clearly illustrate that the inclusion of the foreshocks along with
 639 the earthquake rate models that favour earthquake clustering produces higher probabili-
 640 ties for the occurrence of the largest expected earthquakes during the specified forecast-
 641 ing period of $\Delta T = 7$ days.

642 The 2019 Ridgecrest earthquake sequence bears a striking similarity to the 2016
 643 Kumamoto, Japan, earthquake sequence. Both sequences had a pronounced foreshock
 644 sequence which was triggered by the strong foreshocks of similar magnitudes (M6.4 vs.
 645 M6.5) and duration. They occurred on the different fault segments than the mainshock
 646 fault rupture. The b -values of the GR relation and p values of the OU law were also smaller
 647 than the values for the aftershocks generated by the mainshocks. The mainshock mag-
 648 nitudes were also similar (M7.1 vs. M7.3) and had the strike-slip mechanisms.

649 To validate the three stochastic models, several statistical tests (N-, M-, R-, and
 650 T-tests) were applied retrospectively for several combinations of the training and fore-
 651 casting time intervals. The results of the N-test indicate that the OU model underes-
 652 timated the observed number of earthquakes for most of the forecasting time intervals.
 653 The compound OU model performed better especially in the early stages of the evolu-
 654 tion of the sequence. The ETAS model approximated the observed number of earthquakes
 655 during the all considered forecasting time intervals, however, the ETAS model also had
 656 wider 95% spread in the number of forecasted earthquakes (Figure 10). This is the con-
 657 sequence of the branching nature of the ETAS process and the deviation of the distri-
 658 bution of the number of events from the Poisson distribution. The ETAS model was also
 659 consistent in reproducing the distribution of the magnitudes in each bin that is illustrated
 660 in Figure 11c through the κ quantile score.

661 The comparative analysis of the ETAS model versus the OU and the compound
 662 OU models also confirmed that the forecast based on the ETAS model outperformed the
 663 forecasts based on the other two models. This is illustrated in Figure 12, where the quan-
 664 tile score α from the R-test is plotted at the end of each forecasting time interval. The
 665 values of the score above the threshold level 0.025 indicate that the ETAS model out-
 666 performed the other two models. The similar conclusion is drawn from the plot (Figure 13)
 667 of the sample information gain $I_N(\mathbf{\Lambda}^2, \mathbf{\Lambda}^1)$. The results of the T-test confirmed that the
 668 ETAS model provided a statistically significant information gain with respect to the mod-
 669 els based on the OU or compound OU rates except for the last forecasting interval end-
 670 ing at 38.4284 days, where the ETAS model and the model based on the compound OU
 671 rate performed similarly. For the last forecasting time interval ending at $T_e + \Delta T =$
 672 38.4284 days, there were only two events above magnitude $m \geq 3.2$. The compound
 673 OU model produced relatively close results when computing the probabilities for the oc-
 674 currence of the largest expected earthquakes (Figure 9).

675 One limitation of the above tests (M-, R-, T-) based on the computing of the joint
676 log-likelihoods, equation (14), is that they assume that the distribution of the number
677 of earthquakes in the forecasting time interval is Poisson. This is true for the both point
678 process models based on the OU law. However, the ETAS model deviates from the Pois-
679 son assumption. This was already demonstrated in Shcherbakov et al. (2019) when com-
680 puting the Bayesian predictive distribution. Therefore, the application of these tests to
681 the ETAS based models has to be considered approximate.

682 The above tests implemented in this work used the MCMC sampling of the pos-
683 terior distribution of the model parameters. This allowed to incorporate the stochastic
684 variability of the model parameters and the uncertainty associated with the prior infor-
685 mation on the model parameters into the computation of the resulting probabilities and
686 performing the statistical tests. The consistency of the Bayesian predictive distribution
687 was evaluated by estimating the Bayesian p -value, equation (16). All the three models
688 were consistent in reproducing the observed largest earthquakes in each forecasting time
689 interval.

690 5 Conclusions

691 The 2019 Ridgecrest earthquake sequence was characterized by the complex clus-
692 tering of seismicity with earthquakes occurring on a distributed fault network. It also
693 presented a good opportunity to analyze the sequence retrospectively in order to test sev-
694 eral statistical approaches to study the sequence in temporal and magnitude domains
695 and to forecast the occurrence of the largest expected aftershocks during the evolution
696 of the sequence.

697 The frequency-magnitude statistics of earthquakes were studied for the foreshock
698 and aftershock sequences and modeled using the exponential distribution, equation (2).
699 The earthquake rate was analyzed during predefined time intervals in order to fit the three
700 statistical models to describe its temporal evolution. Specifically, the OU law, equation (4),
701 the compound OU formula, equation (5), and the ETAS model, equation (6), were used.

702 Two approaches were used to compute the probabilities of having the largest ex-
703 pected earthquakes to be above certain magnitudes after specified time intervals and dur-
704 ing the fixed forecasting time interval $\Delta T = 7$ days. For the first approach, the EVD,
705 equation (8), with the OU law, equation (4), or the compound OU formula, equation (5),

706 was used. In the second approach, the Bayesian predictive distribution, equation (11),
707 combined with the OU law or the ETAS model, equation (6), was used. The compar-
708 ison of these approaches are illustrated in Figure 9.

709 Applying these two approaches to the 2019 Ridgecrest earthquake sequence revealed
710 that the incorporation of the foreshock sequence for the subsequent computation of the
711 probabilities to have the largest expected aftershocks above a certain magnitude was im-
712 portant. This was also relevant to the choice of the model to approximate the earthquake
713 rate. Specifically, the compound OU law, equation (5), and the ETAS model, equation (6),
714 provide a better approximation for the earthquake rate than the OU law, equation (4),
715 applied separately to the foreshock and aftershock sequences during the forecasting time
716 intervals. These conclusions have been verified by the several statistical tests. Overall,
717 the ETAS model passed the tests most of the time and was successful in reproducing the
718 observed number of earthquakes and the distribution of magnitudes. Therefore, the com-
719 puted probabilities using the Bayesian predictive distribution (Figure 8) for the largest
720 expected earthquake during the evolution of the 2019 Ridgecrest sequence can be con-
721 sidered accurate.

722 **Data and Resources**

723 The Southern California Seismic Network (SCSN, [https://service.scedc.caltech](https://service.scedc.caltech.edu/eq-catalogs/date_mag_loc.php)
724 [.edu/eq-catalogs/date_mag_loc.php](https://service.scedc.caltech.edu/eq-catalogs/date_mag_loc.php)) database was used for seismicity (last accessed
725 on June 7, 2020).

726 U.S. Geological Survey and California Geological Survey, 2006, Quaternary fault
727 and fold database for the United States, accessed June 7, 2020, from USGS web site:
728 <https://earthquake.usgs.gov/hazards/qfaults/> (last accessed on June 7, 2020).

729 The data analysis was performed using a computer code written in Matlab and can
730 be requested from the author.

731 The Supporting Information for this article includes Tables S1-S3 with the param-
732 eters of the Gamma distribution, which was used as a prior distribution for the param-
733 eters of the three models considered in the work. It also includes plots illustrating the
734 fit of the compound OU (Figure S1) and the ETAS (Figure S2) models. The MCMC sam-
735 pling of the model parameters for the OU (Figures S4-S5), the compound OU (Figures S6-
736 8), the ETAS (Figures S9-S11) models are provided for one specific training and fore-

737 casting time intervals. The additional quantile scores of the plots are given in Figures S12-
738 S15.

739 **Acknowledgments**

740 This work has been supported by the NSERC Discovery grant.

741 **References**

- 742 Barnhart, W. D., Hayes, G. P., & Gold, R. D. (2019). The July 2019 Ridgecrest,
743 California, earthquake sequence: Kinematics of slip and stressing in cross-fault
744 ruptures. *Geophys. Res. Lett.*, *46*, 11859-11867. doi: 10.1029/2019gl084741
- 745 Båth, M. (1965). Lateral inhomogeneities of the upper mantle. *Tectonophysics*, *2*,
746 483-514.
- 747 Bender, B. (1983). Maximum-likelihood estimation of b -values for magnitude
748 grouped data. *Bull. Seismol. Soc. Am.*, *73*(3), 831-851.
- 749 Campbell, K. W. (1982). Bayesian analysis of extreme earthquake occurrences. Part
750 I. Probabilistic hazard model. *Bull. Seismol. Soc. Am.*, *72*(5), 1689-1705.
- 751 Cattania, C., Werner, M. J., Marzocchi, W., Hainzl, S., Rhoades, D., Gerstenberger,
752 M., ... Jordan, T. H. (2018). The forecasting skill of physics-based seismicity
753 models during the 2010-2012 Canterbury, New Zealand, earthquake sequence.
754 *Seismol. Res. Lett.*, *89*(4), 1238-1250. doi: 10.1785/0220180033
- 755 Coles, S. (2001). *An Introduction to Statistical Modeling of Extreme Values*
756 (Vol. 208). London: Springer.
- 757 Console, R., Lombardi, A. M., Murru, M., & Rhoades, D. (2003). Båth's law and
758 the self-similarity of earthquakes. *J. Geophys. Res.*, *108*(B2), 2128. doi: 10
759 .1029/2001JB001651
- 760 Daley, D. J., & Vere-Jones, D. (2003). *An Introduction to the Theory of Point Pro-*
761 *cesses* (2nd ed., Vol. 1). New York: Springer.
- 762 Ebrahimian, H., & Jalayer, F. (2017). Robust seismicity forecasting based on
763 Bayesian parameter estimation for epidemiological spatio-temporal aftershock
764 clustering models. *Sci. Rep.*, *7*, 9803. doi: 10.1038/s41598-017-09962-z
- 765 Ebrahimian, H., Jalayer, F., Asprone, D., Lombardi, A. M., Marzocchi, W., Prota,
766 A., & Manfredi, G. (2014). Adaptive daily forecasting of seismic aftershock
767 hazard. *Bull. Seismol. Soc. Am.*, *104*(1), 145-161. doi: 10.1785/0120130040

- 768 Felzer, K. R., Abercrombie, R. E., & Ekström, G. (2004). A common origin for
 769 aftershocks, foreshocks, and multiplets. *Bull. Seismol. Soc. Am.*, *94*(1), 88-98.
 770 doi: 10.1785/0120030069
- 771 Gelman, A., Carlin, J., Stern, H., Dunson, D., Vehtari, A., & Rubin, D. (2013).
 772 *Bayesian data analysis* (3rd ed.). CRC Press.
- 773 Gerstenberger, M. C., Marzocchi, W., Allen, T., Pagani, M., Adams, J., Danciu, L.,
 774 ... Petersen, M. D. (2020). Probabilistic seismic hazard analysis at regional
 775 and national scale: State of the art and future challenges. *Rev. Geophys.*,
 776 e2019RG000653. doi: 10.1029/2019rg000653
- 777 Gerstenberger, M. C., Wiemer, S., Jones, L. M., & Reasenberg, P. A. (2005). Real-
 778 time forecasts of tomorrow's earthquakes in California. *Nature*, *435*(7040),
 779 328-331. doi: 10.1038/Nature03622
- 780 Gutenberg, B., & Richter, C. F. (1944). Frequency of earthquakes in California.
 781 *Bull. Seismol. Soc. Am.*, *4*, 185-188.
- 782 Hainzl, S. (2016a). Apparent triggering function of aftershocks resulting from rate-
 783 dependent incompleteness of earthquake catalogs. *J. Geophys. Res.*, *121*(9),
 784 6499-6509. doi: 10.1002/2016jb013319
- 785 Hainzl, S. (2016b). Rate-dependent incompleteness of earthquake catalogs. *Seismol.*
 786 *Res. Lett.*, *87*(2), 337-344. doi: 10.1785/0220150211
- 787 Hardebeck, J. L., Llenos, A. L., Michael, A. J., Page, M. T., & van der Elst, N.
 788 (2019). Updated California aftershock parameters. *Seismol. Res. Lett.*, *90*(1),
 789 262-270. doi: 10.1785/0220180240
- 790 Harte, D. (2010). PtProcess: An R package for modelling marked point process in-
 791 dexed by time. *J. Stat. Softw.*, *35*(8), 1-32.
- 792 Harte, D. S. (2017). Probability distribution of forecasts based on the ETAS model.
 793 *Geophys. J. Int.*, *210*(1), 90-104. doi: 10.1093/gji/ggx146
- 794 Helmstetter, A., Kagan, Y. Y., & Jackson, D. D. (2006). Comparison of short-term
 795 and time-independent earthquake forecast models for southern California. *Bull.*
 796 *Seismol. Soc. Am.*, *96*(1), 90-106. doi: 10.1785/0120050067
- 797 Kagan, Y. Y. (2004). Short-term properties of earthquake catalogs and models of
 798 earthquake source. *Bull. Seismol. Soc. Am.*, *94*(4), 1207-1228.
- 799 Kagan, Y. Y., & Jackson, D. D. (1995). New seismic gap hypothesis: Five years af-
 800 ter. *J. Geophys. Res.*, *100*(B3), 3943-3959. doi: 10.1029/94jb03014

- 801 Liu, C. L., Lay, T., Brodsky, E. E., Dascher-Cousineau, K., & Xiong, X. (2019).
 802 Coseismic rupture process of the large 2019 Ridgecrest earthquakes from joint
 803 inversion of geodetic and seismological observations. *Geophys. Res. Lett.*, *46*,
 804 11820-11829. doi: 10.1029/2019gl084949
- 805 Michael, A. J., McBride, S. K., Hardebeck, J. L., Barall, M., Martinez, E., Page,
 806 M. T., ... Wein, A. M. (2019). Statistical seismology and communication of
 807 the USGS operational aftershock forecasts for the 30 November 2018 Mw 7.1
 808 Anchorage, Alaska, earthquake. *Seismol. Res. Lett.*, *91*(1), 153-173. doi:
 809 10.1785/0220190196
- 810 Nanjo, K. Z., Tsuruoka, H., Yokoi, S., Ogata, Y., Falcone, G., Hirata, N., ...
 811 Zhuang, J. (2012). Predictability study on the aftershock sequence follow-
 812 ing the 2011 Tohoku-Oki, Japan, earthquake: first results. *Geophys. J. Int.*,
 813 *191*(2), 653-658. doi: 10.1111/j.1365-246X.2012.05626.x
- 814 Ogata, Y. (1983). Estimation of the parameters in the modified Omori formula for
 815 aftershock frequencies by the maximum-likelihood procedure. *J. Phys. Earth*,
 816 *31*(2), 115-124. doi: 10.4294/jpe1952.31.115
- 817 Ogata, Y. (1988). Statistical-models for earthquake occurrences and residual analy-
 818 sis for point-processes. *J. Am. Stat. Assoc.*, *83*(401), 9-27.
- 819 Ogata, Y. (1999). Seismicity analysis through point-process modeling: A review.
 820 *Pure Appl. Geophys.*, *155*(2-4), 471-507.
- 821 Ogata, Y. (2017). Statistics of earthquake activity: Models and methods for earth-
 822 quake predictability studies. *Annu. Rev. Earth Planet. Sci.*, *45*, 497-527. doi:
 823 10.1146/annurev-earth-063016-015918
- 824 Omi, T., Ogata, Y., Hirata, Y., & Aihara, K. (2013). Forecasting large af-
 825 tershocks within one day after the main shock. *Sci. Rep.*, *3*, 2218. doi:
 826 10.1038/srep02218
- 827 Omi, T., Ogata, Y., Hirata, Y., & Aihara, K. (2014). Estimating the ETAS model
 828 from an early aftershock sequence. *Geophys. Res. Lett.*, *41*(3), 850-857. doi: 10
 829 .1002/2013gl058958
- 830 Omi, T., Ogata, Y., Shiomi, K., Enescu, B., Sawazaki, K., & Aihara, K. (2016). Au-
 831 tomatic aftershock forecasting: A test using real-time seismicity data in Japan.
 832 *Bull. Seismol. Soc. Am.*, *106*(6), 2450-2458. doi: 10.1785/0120160100
- 833 Omi, T., Ogata, Y., Shiomi, K., Enescu, B., Sawazaki, K., & Aihara, K. (2019).

- 834 Implementation of a real-time system for automatic aftershock forecasting in
 835 Japan. *Seismol. Res. Lett.*, *90*, 242-250. doi: 10.1785/0220180213
- 836 Omori, F. (1894). On after-shocks of earthquakes. *J. Coll. Sci. Imp. Univ. Tokyo*, *7*,
 837 113-200.
- 838 Page, M. T., van der Elst, N., Hardebeck, J., Felzer, K., & Michael, A. J. (2016).
 839 Three ingredients for improved global aftershock forecasts: Tectonic region,
 840 time-dependent catalog incompleteness, and intersequence variability. *Bull.*
 841 *Seismol. Soc. Am.*, *106*(5), 2290-2301. doi: 10.1785/0120160073
- 842 Peng, Z. G., Vidale, J. E., & Houston, H. (2006). Anomalous early aftershock decay
 843 rate of the 2004 Mw 6.0 Parkfield, California, earthquake. *Geophys. Res. Lett.*,
 844 *33*(17), L17307. doi: 10.1029/2006GL026744
- 845 Reasenber, P. A., & Jones, L. M. (1989). Earthquake hazard after a mainshock in
 846 California. *Science*, *243*(4895), 1173-1176.
- 847 Renard, B., Sun, X., & Lang, M. (2013). Bayesian methods for non-stationary ex-
 848 treme value analysis. In A. AghaKouchak, D. Easterling, K. Hsu, S. Schubert,
 849 & S. Sorooshian (Eds.), *Extremes in a changing climate: Detection, analysis*
 850 *and uncertainty* (p. 39-95). Dordrecht: Springer.
- 851 Rhoades, D. A., Christophersen, A., Gerstenberger, M. C., Liukis, M., Silva, F.,
 852 Marzocchi, W., . . . Jordan, T. H. (2018). Highlights from the first ten years of
 853 the New Zealand earthquake forecast testing center. *Seismol. Res. Lett.*, *89*(4),
 854 1229-1237. doi: 10.1785/0220180032
- 855 Rhoades, D. A., Liukis, M., Christophersen, A., & Gerstenberger, M. C. (2016).
 856 Retrospective tests of hybrid operational earthquake forecasting models for
 857 Canterbury. *Geophys. J. Int.*, *204*(1), 440-456. doi: 10.1093/gji/ggv447
- 858 Rhoades, D. A., Schorlemmer, D., Gerstenberger, M. C., Christophersen, A., Zechar,
 859 J. D., & Imoto, M. (2011). Efficient testing of earthquake forecasting models.
 860 *Acta Geophys.*, *59*(4), 728-747. doi: 10.2478/s11600-011-0013-5
- 861 Ross, Z. E., Idini, B., Jia, Z., Stephenson, O. L., Zhong, M. Y., Wang, X., . . .
 862 Jung, J. (2019). Hierarchical interlocked orthogonal faulting in the
 863 2019 Ridgecrest earthquake sequence. *Science*, *366*(6463), 346-351. doi:
 864 10.1126/science.aaz0109
- 865 Schorlemmer, D., Gerstenberger, M. C., Wiemer, S., Jackson, D. D., & Rhoades,
 866 D. A. (2007). Earthquake likelihood model testing. *Seismol. Res. Lett.*, *78*(1),

- 867 17-29. doi: 10.1785/gssrl.78.1.17
- 868 Schorlemmer, D., Werner, M. J., Marzocchi, W., Jordan, T. H., Ogata, Y., Jackson,
869 D. D., ... Zhuang, J. C. (2018). The collaboratory for the study of earth-
870 quake predictability: Achievements and priorities. *Seismol. Res. Lett.*, *89*(4),
871 1305-1313. doi: 10.1785/0220180053
- 872 Shcherbakov, R., Goda, K., Iwanian, A., & Atkinson, G. M. (2013). Aftershock
873 statistics of major subduction earthquakes. *Bull. Seismol. Soc. Am.*, *103*(6),
874 3222-3234. doi: 10.1785/0120120337
- 875 Shcherbakov, R., Nguyen, M., & Quigley, M. (2012). Statistical analysis of the 2010
876 Mw 7.1 Darfield earthquake aftershock sequence. *New Zealand J. Geol. Geo-
877 phys.*, *55*(3), 305-311. doi: 10.1080/00288306.2012.676556
- 878 Shcherbakov, R., & Turcotte, D. L. (2004). A modified form of Båth's law. *Bull.
879 Seismol. Soc. Am.*, *94*(5), 1968-1975. doi: 10.1785/012003162
- 880 Shcherbakov, R., Turcotte, D. L., & Rundle, J. B. (2004). A generalized Omori's law
881 for earthquake aftershock decay. *Geophys. Res. Lett.*, *31*(11), L11613. doi: 10
882 .1029/2004GL019808
- 883 Shcherbakov, R., Turcotte, D. L., & Rundle, J. B. (2005). Aftershock statistics. *Pure
884 Appl. Geophys.*, *162*(6-7), 1051-1076. doi: 10.1007/s00024-004-2661-8
- 885 Shcherbakov, R., Turcotte, D. L., & Rundle, J. B. (2006). Scaling properties of the
886 Parkfield aftershock sequence. *Bull. Seismol. Soc. Am.*, *96*(4B), S376-384. doi:
887 10.1785/0120050815
- 888 Shcherbakov, R., Turcotte, D. L., & Rundle, J. B. (2015). Complexity and earth-
889 quakes. In H. Kanamori (Ed.), *Earthquake seismology* (2nd ed., Vol. 4, p. 627-
890 653). Elsevier.
- 891 Shcherbakov, R., Yakovlev, G., Turcotte, D. L., & Rundle, J. B. (2005). Model
892 for the distribution of aftershock interoccurrence times. *Phys. Rev. Lett.*, *95*,
893 218501. doi: 10.1103/PhysRevLett.95.218501
- 894 Shcherbakov, R., Zhuang, J., & Ogata, Y. (2018). Constraining the magnitude of the
895 largest event in a foreshock-mainshock-aftershock sequence. *Geophys. J. Int.*,
896 *212*(1), 1-13. doi: 10.1093/gji/ggx407
- 897 Shcherbakov, R., Zhuang, J., Zöller, G., & Ogata, Y. (2019). Forecasting the mag-
898 nitude of the largest expected earthquake. *Nat. Commun.*, *10*, Art. 4051. doi:
899 10.1038/s41467-019-11958-4

- 900 Shearer, P. M. (2012). Self-similar earthquake triggering, Båth's law, and fore-
 901 shock/aftershock magnitudes: Simulations, theory, and results for southern
 902 California. *J. Geophys. Res.*, *117*, B06310. doi: 10.1029/2011jb008957
- 903 Shebalin, P., Narteau, C., Holschneider, M., & Schorlemmer, D. (2011). Short-term
 904 earthquake forecasting using early aftershock statistics. *Bull. Seismol. Soc.*
 905 *Am.*, *101*(1), 297-312. doi: 10.1785/0120100119
- 906 Tahir, M., Grasso, J. R., & Amorese, D. (2012). The largest aftershock: How strong,
 907 how far away, how delayed? *Geophys. Res. Lett.*, *39*, L04301. doi: 10.1029/
 908 2011gl050604
- 909 Taroni, M., Marzocchi, W., Schorlemmer, D., Werner, M. J., Wiemer, S., Zechar,
 910 J. D., ... Euchner, F. (2018). Prospective CSEP evaluation of 1-day, 3-month,
 911 and 5-yr earthquake forecasts for Italy. *Seismol. Res. Lett.*, *89*(4), 1251-1261.
 912 doi: 10.1785/0220180031
- 913 Tinti, S., & Mulargia, F. (1987). Confidence intervals of *b*-values for grouped magni-
 914 tudes. *Bull. Seismol. Soc. Am.*, *77*(6), 2125-2134.
- 915 Utsu, T. (1961). A statistical study on the occurrence of aftershocks. *Geophys.*
 916 *Mag.*, *30*, 521-605.
- 917 Utsu, T., Ogata, Y., & Matsu'ura, R. S. (1995). The centenary of the Omori formula
 918 for a decay law of aftershock activity. *J. Phys. Earth*, *43*(1), 1-33.
- 919 Vere-Jones, D. (1969). A note on the statistical interpretation of Båth's law. *Bull.*
 920 *Seismol. Soc. Am.*, *59*, 1535-1541.
- 921 Vere-Jones, D. (1975). Stochastic models for earthquake sequences. *Geophys. J. Int.*,
 922 *42*(2), 811-826. doi: 10.1111/j.1365-246X.1975.tb05893.x
- 923 Vere-Jones, D. (2010). Foundations of statistical seismology. *Pure Appl. Geophys.*,
 924 *167*(6-7), 645-653. doi: 10.1007/s00024-010-0079-z
- 925 Zechar, J. D., Gerstenberger, M. C., & Rhoades, D. A. (2010). Likelihood-based
 926 tests for evaluating space-rate-magnitude earthquake forecasts. *Bull. Seismol.*
 927 *Soc. Am.*, *100*(3), 1184-1195. doi: 10.1785/0120090192
- 928 Zöller, G., Holschneider, M., & Hainzl, S. (2013). The maximum earthquake mag-
 929 nitude in a time horizon: Theory and case studies. *Bull. Seismol. Soc. Am.*,
 930 *103*(2A), 860-875. doi: 10.1785/0120120013